A computational investigation of the phase behavior and capillary sublimation of water confined between nanoscale hydrophobic plates

Andrew L. Ferguson, Nicolás Giovambattista, Peter J. Rossky, Athanassios Z. Panagiotopoulos, and Pablo G. Debenedetti

Citation: J. Chem. Phys. **137**, 144501 (2012); doi: 10.1063/1.4755750
View online: http://dx.doi.org/10.1063/1.4755750
View Table of Contents: http://jcp.aip.org/resource/1/JCPSA6/v137/i14
Published by the American Institute of Physics.

A computational investigation of the phase behavior and capillary sublimation of water confined between nanoscale hydrophobic plates

Andrew L. Ferguson,[1,a)] Nicolás Giovambattista,[2] Peter J. Rossky,[3]
Athanassios Z. Panagiotopoulos,[4] and Pablo G. Debenedetti[4]
[1]*Department of Materials Science and Engineering, University of Illinois, Urbana, Illinois 61801, USA*
[2]*Department of Physics, Brooklyn College of the City University of New York, Brooklyn, New York 11210, USA*
[3]*Department of Chemistry and Biochemistry, University of Texas, Austin, Texas 78712, USA*
[4]*Department of Chemical and Biological Engineering, Princeton University, Princeton, New Jersey 08544, USA*

(Received 27 June 2012; accepted 5 September 2012; published online 8 October 2012)

Thin films of water under nanoscopic confinement are prevalent in natural and manufactured materials. To investigate the equilibrium and dynamic behavior of water in such environments, we perform molecular dynamics simulations of water confined between atomistically detailed hydrophobic plates at $T = 298$ K for pressures $(-0.1) \leq P \leq 1.0$ GPa and plate separations of $0.40 \leq d \leq 0.80$ nm. From these simulations, we construct an expanded P-d phase diagram for confined water, and identify and characterize a previously unreported confined monolayer ice morphology. We also study the decompression-induced sublimation of bilayer ice in a $d = 0.6$ nm slit, employing principal component analysis to synthesize low-dimensional embeddings of the drying trajectories and develop insight into the sublimation mechanism. Drying is observed to proceed by the nucleation of a bridging vapor cavity at one corner of the crystalline slab, followed by expansion of the cavity along two edges of the plates, and the subsequent recession of the remaining promontory of bilayer crystal into the bulk fluid. Our findings have implications for the understanding of diverse phenomena in materials science, nanofluidics, and protein folding and aggregation. © *2012 American Institute of Physics*. [http://dx.doi.org/10.1063/1.4755750]

I. INTRODUCTION

The equilibrium and dynamic behavior of thin water films between confining surfaces is of fundamental scientific interest due to the varied and unexpected behavior that arise as the confining length scale approaches a few molecular diameters.[1–3] Systems consisting of thin water films are frequently encountered in natural and engineered materials, including zeolites and clays,[4] hydrogels,[5] ion channels,[6] carbon nanotubes,[7] proteins,[8] and microfluidic devices.[9] Accordingly, the study of the equilibrium phase behavior of confined water is of practical importance in applications ranging from catalysis[10] and corrosion prevention,[11] to self-assembly[1] and protein folding.[12] Confinement disrupts the hydrogen bonding network observed in bulk water, thereby suppressing the onset of crystal nucleation below the bulk homogeneous nucleation temperature. In principle, therefore, confined systems present an elegant avenue to the experimental and theoretical study of supercooled water at otherwise inaccessible temperatures.[13,14] At present, however, the usefulness of this approach is limited by a lack of fundamental understanding of the relationship between observed behavior in nanoscale confinement and implied behavior in the bulk. Calculations such as those reported in this work contribute to filling gaps in this understanding that may eventually permit the unambiguous experimental testing of competing theoretical pictures of the origin of the anomalous thermodynamic and dynamic properties of water in the supercooled regime.[13–18]

Stillinger's seminal 1973 paper describing the behavior of water in the vicinity of nonpolar solutes inspired numerous investigations into the thermodynamic and dynamic properties of water near or between hydrophobic surfaces.[19] The drying transition of water confined between hydrophobic surfaces is now understood to be an important factor in phenomena as diverse as amphiphile and membrane self-assembly,[20] the association of hydrophobic particles,[1] hydrophobic polymer collapse,[21,22] the structure and solubility of *n*-alkane chains,[23,24] cavitation inhibition,[25] and protein folding and assembly.[26–31] The first simulations of the drying transition were reported by Luzar, Bratko, and Blum in 1987, who conducted grand canonical Monte Carlo simulations of a hard sphere water model with an embedded dipole and orientation dependent attraction between infinite hard walls.[32] Subsequent work by Bérard *et al.* for a Lennard-Jones fluid between hard walls[33] demonstrated capillary evaporation to be the result of comparatively weak fluid-wall attractions relative to fluid-fluid interactions,[2,34] and therefore not restricted to water.[35] Nevertheless, most published works have employed water as the confined fluid due to its ubiquity, intriguing thermophysical property anomalies and biophysical relevance.[15] Many studies have investigated the thermodynamics of the drying transition,[14,34,36–43] with recent work focusing on the role of surface hydrophilicity and heterogeneity.[25,29,34,44–49] Comparatively fewer studies have addressed the dynamical and mechanistic aspects of capillary

a)Author to whom correspondence should be addressed. Electronic mail: alf@illinois.edu. Tel.: (217) 300-2354. Fax.: (217) 333-2736.

evaporation,[50–56] and, to our knowledge, none has considered the sublimation of confined ice.

Capillary drying is an activated process with free energy barriers in excess of several k_BT even for surfaces separated by nanometer length scales,[38,51,53] making the observation of drying transitions a rare event requiring sophisticated sampling techniques[50,51] or coarse-grained computational models.[54] Theoretical arguments[57] and computer simulations[56] strongly support the view whereby capillary evaporation proceeds by the nucleation of a vapor tube that bridges the gap between the surfaces as an hourglass shaped cavity, and which subsequently expands to fill the entire gap region and expel the inter-plate water molecules.[1,3,50,51,54,58] Experimental evidence for this mechanism, however, is conflicting and inconclusive.[58–69]

In Glauber Monte Carlo simulations of a water-like lattice gas between hydrophobic walls, Lum and Luzar observed the formation of the bridging cavity to be preceded by capillary wave fluctuations in the vapor-liquid interface.[54] Bolhuis and Chandler performed transition path sampling of the evaporation of a Lennard-Jones fluid confined by Weeks-Chandler-Andersen discs, and identified the volume and radius of the vapor cavity as relevant reaction coordinates. They further determined the transition state ensemble to be populated by configurations with a "critical vapor nucleus".[50] Leung and Luzar corroborated the cavity size as a good reaction coordinate using umbrella sampling Monte Carlo of the lattice gas model, and identified fluctuations in cavity size as an important additional reaction coordinate.[52] Luzar subsequently showed the activation barrier for drying to scale with plate separation with an exponent of 1.9 ± 0.1 in lattice gas simulations,[53] while Leung *et al.* employed the realistic SPC water model in a grand canonical Monte Carlo study, coupled with reactive flux molecular dynamics simulations, to quantify the activation barriers and evaporation rates for the formation of the bridging vapor cavity.[51] Huang *et al.* observed capillary evaporation of liquid SPC water from between Gay-Berne ellipsoids to proceed by bridging cavity nucleation, but did not study the mechanism of this event.[1] More recently, the thermodynamics and kinetics of the vapor-liquid phase transition for water in nanoscopic hydrophobic confinement has been explored by Xu and Molinero using a coarse-grained water model,[55] while Sharma and Debenedetti employed forward flux sampling to calculate the rates and free energy barriers for capillary evaporation.[56]

The principal objectives of the current study are twofold. Our first goal is to map the room temperature phase behavior of nanoscopically confined water between hydrophobic surfaces to higher pressures, and with higher resolution in pressure and plate separation than previously reported.[34,42] Through extensive molecular dynamics simulations, we provide a detailed thermodynamic and dynamic characterization of the six different "wet" phases of confined water observed in this study, and report the existence of heretofore unobserved hexagonal monolayer ice. Our second objective is to investigate the microscopic sublimation mechanism of a confined bilayer ice. We employ linear dimensionality reduction to parametrize the drying transition in a small number of physically interpretable collective modes, to provide a low-dimensional representation of the drying trajectories and develop insight into the dynamical mechanism. To the best of our knowledge, this work represents the first study of the ice to vapor sublimation transition in a nanoscale confined system.

The organization of this paper is as follows. In Sec. II we describe the details of our equilibrium and non-equilibrium molecular dynamics simulations, techniques for structural and dynamical characterization of the observed morphologies, and the dimensionality reduction approach employed to analyze the sublimation transition. In Sec. III we present an expanded phase diagram for water under confinement, and we analyze in detail the bilayer ice to vapor sublimation transition. In Sec. IV we summarize the principal conclusions and implications of this work, and outline additional studies suggested by our results.

II. COMPUTATIONAL AND THEORETICAL METHODS

In this section, we describe the elements of our methodology used to carry out the characterization of confined water samples. These elements include basic simulation algorithms that we implemented, definition of conventional and unconventional structural and dynamical quantities calculated, and the novel methods brought to bear on understanding the non-equilibrium dynamics of phase changes.

A. Equilibrium simulations of nanoscopically confined water

We performed molecular dynamics simulations using the GROMACS simulation package[70,71] to explore the phase behavior of water confined between atomistically detailed hydrophobic plates. Employing the geometry previously studied by Giovambattista *et al.*,[34,45] two identical silica plates, each comprising 196 Si and 478 O atoms arranged in four SiO_2 layers corresponding to the (1.1.1) octahedral cristobalite face,[72,73] were placed in a 5.5 nm cubic box parallel to the *y*,*z*-plane, as illustrated in Fig. 1. All molecular visualizations in this work were generated using the VMD software package.[74] We chose to employ finite, rather than infinite,[75] plates, to provide a more seamless integration with our investigation of the mechanism of capillary evaporation, which requires a pathway for the confined water to escape into the bulk. Accordingly, our system does not possess strict translational invariance in any dimension due to the finite nature of the plates. The SiO_2 unit cell was modeled as an ideal tetrahedron with Si-O and O-O interatomic distances equal to 0.151 nm and 0.247 nm, respectively. The system was solvated by attempting random insertions of SPC/E[76] water molecules throughout the box, until 4956 solvent molecules were introduced while avoiding overlap with any existing van der Waals radii.

For consistency with previously established convention,[34,45] the plate separation, d, was defined as the distance between the (imaginary) plane of H atoms that would be formed by hydroxylating each surface SiO_2 group by the addition of an H atom with Si-H bond length 0.1 nm and Si-O-H bond angle 109.27°. This hypothetical plane lies

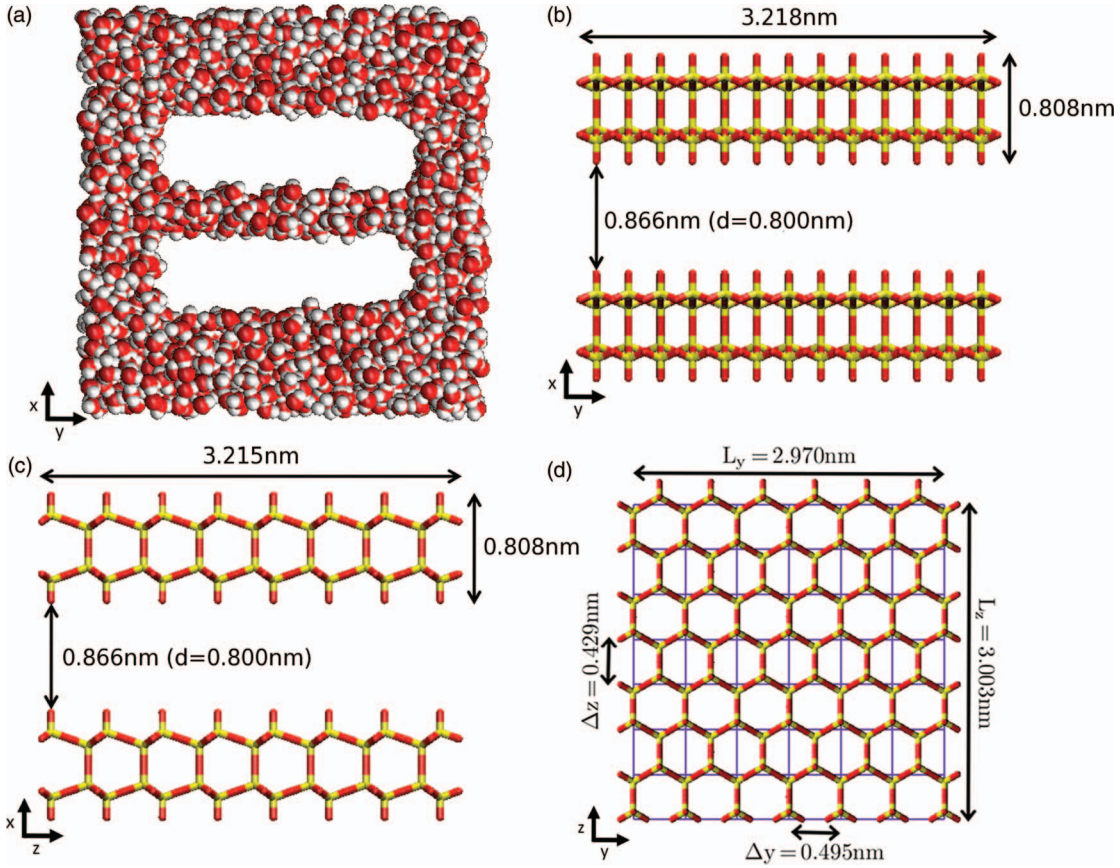

FIG. 1. Illustration of the simulated system. Throughout this work, unless otherwise stated, oxygen atoms are colored red, hydrogen white, and silicon yellow. (a) Two identical silica plates were solvated in an initially 5.5 nm cubic box of SPC/E water, and immobilized at a particular separation in the x-direction to form a planar gap of fixed width. The vacant regions in this x,y-projection illustrate the position of the plates, between which resides a slab of confined water. (b) and (c) Tranverse views of the plates. For reasons described in the main text, the gap width, d, is defined as 0.066 nm greater than the linear separation between the plane containing the innermost layer of O atoms in each plate. (d) Plan view of the plates. The gap region was discretized into 42 cubic cells of dimensions [$\Delta y = 0.495$ nm, $\Delta z = 0.429$ nm], which span the gap in the x-direction. A coarse-grained characterization of a particular system configuration was developed for the purposes of linear dimensionality reduction by enumerating the water molecules residing within each cell, to synthesize what we term the occupancy vector of the gap.

0.033 nm above that containing the surface O atoms,[45] so that a reported plate separation of d corresponds to a distance ($d + 0.066$) nm between the O atom planes (Fig. 1). The gap between the plates was formed by taking two identically overlapping plates, and displacing one relative to the other by translation in the x-direction. Accordingly, the bottom surface of the upper plate is a mirror image of the upper surface of the bottom plate, and the surface O atoms are in perfect registry. Plate separations in the range 0.40–0.80 nm were considered in increments of 0.05 nm. It has previously been shown that water molecules residing in the gap between plates with $d < 0.4$ nm are immobilized between the plates.[34]

The atoms of the silica plates were frozen in place during the simulation, permitting all intraplate bonded and nonbonded interactions to be neglected. By treating the plate atoms as spatially fixed, we ignore the oscillations of the Si and O atoms around their equilibrium locations. The effect of these vibrational modes upon the phase behavior and drying mechanism of the confined water was not explored, but Giovambattista *et al.* have previously employed the Lindemann criterion to place an upper bound of 0.05 nm on the oscillation amplitude, which is approximately an order of magnitude less than the narrowest plate separation explored in this work.[34] Pairwise non-bonded dispersion interactions within the solvent, and between the solvent and the plates, were modeled using the standard Lennard-Jones 12-6 potential.[77] The ϵ and σ parameters for interactions between the SPC/E water molecules and the Si and O plate atoms were set equal to those employed by Giovambattista *et al.*[34,45] and Lee and Rossky.[78] Each plate atom carried zero partial charge, rendering the plates electrostatically neutral.

High energy unphysical atomic overlaps were first removed by performing steepest descent energy minimization, followed by a short 5 ps NVT simulation to relax the system prior to introducing pressure coupling. Production runs were conducted in the NPT ensemble using a Nosé-Hoover thermostat[79,80] and a Berendsen barostat.[81] The barostat maintained the average system pressure, specifically the mean of the trace of the pressure tensor, by isotropically rescaling the volume of the cubic simulation box.[82] While the size of the simulation box fluctuated during the run, the plates and their relative separation spacing remained fixed. The solvent temperature was maintained at 298 K, and system pressures of (−0.10) to 1.0 GPa were explored. Periodic boundary conditions were employed in all dimensions.

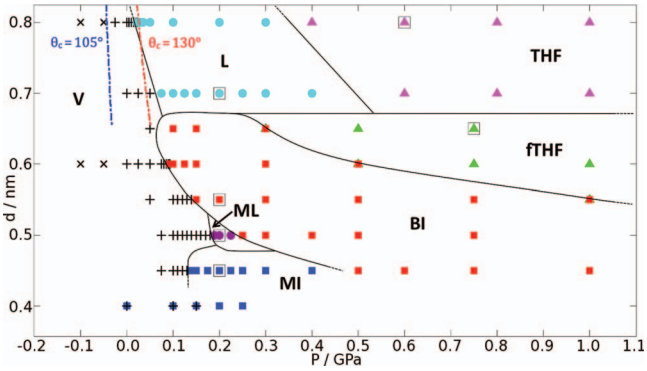

FIG. 2. *P-d* phase diagram for water confined between atomistically detailed hydrophobic plates at $T = 298$ K. Seven different phases of confined water were observed: L—liquid (cyan circles), ML—monolayer liquid (purple circles), BI—bilayer ice (red squares), MI—monolayer ice (blue squares), THF—trilayer heterogeneous fluid (pink triangles), fTHF—frustrated trilayer heterogeneous fluid (green triangles), and V—vapor (black crosses). In the vapor phase region, the + symbols correspond to an effective vacuum between the plates, whereas the × symbols correspond to state points in which cavitation was observed in the fluid surrounding the plates, indicating thermodynamic instability of the bulk liquid under these conditions. The structural and dynamical behavior of each "wet" morphology was characterized in detail at one particular state point indicated by the open squares in the diagram. Superposition of two phase-characterizing symbols (e.g., red squares (BI) and green triangles (fTHF)) indicates the observation of phase coexistence in simulations conducted at this state point. The solid lines demarcate a tentative phase map, but are intended primarily as a guide to the eye rather than a precise localization of the phase boundaries. The dashed extension of these lines indicates projected extrapolations into regions of *P-d* space where simulations were not conducted, or the results were too ambiguous to clearly delineate the phase behavior. Employing the contact angle of $\theta_c = 105°$ computed for this system by Giovambattista *et al.*,[102] the blue dotted-dashed line represents the vapor-liquid phase boundary predicted by Eq. (2) over the range of plate separations for which we observe a vapor-liquid phase transition. Treating the contact angle as an adjustable parameter, the predictions of Eq. (2) show relatively good agreement with the observed boundary for $\theta_c = 130°$, as illustrated by the red dotted-dashed line. The bilayer ice to vapor transition at [$P \approx 0.093$ GPa, $d = 0.60$ nm] was investigated by the analysis of decompression-induced sublimation across this phase boundary.

The equations of motion were integrated using the leap frog algorithm[83] with a time step of 2 fs. Non-bonded Lennard-Jones interactions were smoothly switched to zero at a cutoff of 1.1 nm, while electrostatic interactions were treated using the Particle Mesh Ewald method[84] with a real space cutoff of 1.2 nm and a reciprocal space grid spacing of 0.12. The side length of the simulation box was observed to remain above 5.0 nm for all conditions considered, and the plate separation through the *y*,*z*-plane periodic boundary remained in excess of 2.45 nm.

Simulations were conducted for 5 ns at 119 combinations of pressure and plate spacing to extend the exploration of the low ($\leq$0.80 nm) *d* region of the *P-d* phase diagram in Ref. 34 to higher pressures, and with higher *d* resolution. The specific *P-d* state points explored and the resulting phase diagram are presented in Fig. 2.

B. Characterization of confined morphologies

The static and dynamic equilibrium behavior of the water confined between the plates was characterized by the three metrics previously employed by Giovambattista *et al.*[34] The structure of the confined morphology was quantified by computing the probability density functions (pdfs) for the observation of a water molecule in the *x*-direction across the gap $P_{O,\,gap}(x)$. Bin widths of 0.005 nm were employed, and binning of the water molecules performed with respect to the O atom. A second structural metric was furnished by computing the radial distribution function (rdf), $g_{O,\,gap}(r)$ between the O atoms of the water molecules within the gap region, using a bin size of $\Delta r = 0.001$ nm. Unlike Ref. 34, we choose to employ the Euclidean distance between molecules, *r*, rather than the projection of this distance onto the *y*,*z*-plane, parallel to the hydrophobic surface. We normalize the rdf with respect to a cylindrical volume[85] of radius *r* and height *d* containing water at the mean inter-plate density observed over the course of the equilibrated portion of the simulation. The gap volume was simply calculated from the geometry of the plates as $(3.218 \times 3.215 \times d)$ nm^3 (cf. Fig. 1). Although the choice of cylindrical normalization does not precisely reflect the geometry of the gap, all observed phases contained between only one and three layers of water, and it is a reasonable choice for gaps with $d \ll r$. We note that the finite nature of the gap region causes $g_{O,\,gap}(r)$ to approach zero at large *r*.

A previously unreported monolayer ice phase was observed at plate separations of $d = 0.45$ nm in the approximate pressure range between 0.15 and 0.45 GPa, for which additional structural characterization was performed. Firstly, pdfs of H atom *x*-coordinates of the water molecules residing within the gap, $P_{H,\,gap}(x)$, were compiled in an identical manner to that described above for O atoms. Secondly, the angle of inclination of each of the two O-H vectors with respect to the *y*,*z*-plane was computed for each water molecule within the gap, and pdfs compiled in these two angles, θ_1 and θ_2.

Statistics for all metrics considered were collected over the final 4 ns of the 5 ns production runs, and averaged over all water molecules residing within the gap region in each simulation snapshot. Plots of $P_{O,\,gap}(x)$ and $g_{O,\,gap}(r)$ for the boxed state points in Fig. 2 are presented in Figs. 4 and 5, respectively. For the monolayer ice phase at [$P = 0.20$ GPa, $d = 0.45$ nm], $P_{H,\,gap}(x)$ and the θ angle pdfs are given in Figs. 8 and 9, respectively.

A dynamical equilibrium characterization of the confined phases was carried out by computing the diffusion coefficient of the confined water molecules as a function of transverse gap position, $D(x)$, using a modified Einstein relation approach.[86,87] In this procedure, the gap region is divided into slabs parallel to the surface of the plates, and the mean squared displacement (MSD) computed within each slab. Statistics are accumulated by harvesting from the equilibrated simulation trajectory all single molecule trajectories of length *t* for which a molecule remains within a slab for the entire period, and averaging the molecular displacement over all samples. By repeating this procedure for a range of *t*, the MSD as a function of time may be computed. Treating each slab as quasi-2D, the Einstein relation may be applied in the linear regime to provide an estimate of the diffusivity.[86] Due to mixing between slabs, the number of molecular trajectories remaining within a slab for the entire time period rapidly diminishes with increasing time, motivating us to

perform long, 20 ns simulations, at the six boxed state points in Fig. 2 for which this analysis was done. In each instance we partitioned the inter-plate region into a number of equally sized slabs commensurate with the observed number of water layers within the confined phase. Finally, we note that the symmetry of the confined region permits averaging of the results for slabs equidistant from either the upper or lower plate. In this work, however, we chose not to perform this averaging, instead exploiting the observed emergence of approximate symmetry in $D(x)$ about the mid-plane as an internal consistency check that our measurements have converged. Plots of $D(x)$ for the boxed state points in Fig. 2 are presented in Fig. 6.

C. Decompression-induced capillary evaporation

The mechanism of capillary evaporation was studied for the bilayer ice to vapor sublimation transition at [$P \approx 0.093$ GPa, $d = 0.60$ nm] on the P-d phase diagram in Fig. 2. An equilibrated configuration to the right of the phase boundary with a filled gap region was induced to sublimate by applying a pressure drop to drive the system across the boundary and into the vapor phase. A 15 ns simulation was conducted at the state point [$P = 0.095$ GPa, $d = 0.60$ nm] to provide an ensemble of equilibrated system snapshots to use as the initial states for the evaporation simulations. Configurations at 50 ps intervals were harvested from this trajectory after allowing the full first 5 ns for system equilibration, and used to initialize 201 evaporation simulations in which the pressure was dropped to (-0.025) GPa using a Berendsen barostat with a time constant $\tau_p = 25$ ps. All other simulation parameters were maintained at the values employed in the equilibrium simulations described above. Runs were conducted for 2 ns and configurations saved every 2 ps for analysis. Complete drying of the inter-plate region by the end of the 2 ns trajectory was observed in 117, and partial drying in 63, of the 201 simulations.

We note that the evaporation observed in our simulations is an irreversible transition in which a large pressure drop renders the initial bilayer ice metastable and drives the system into the equilibrium vapor phase. Our choice of a relatively large pressure drop of $\Delta P = (-0.12)$ GPa was constrained by computational considerations, which dictated that the sublimation transition be robustly attainable on nanosecond time scales. The requirement for a substantial pressure drop is consistent with simulations of liquid SPC water confined between smooth hydrophobic plates at separations of 1.25 nm at 298 K and 1 atm by Leung *et al.*, who report a 14.5 k_BT free energy barrier for evaporation, and an average waiting time of 0.8 ± 0.1 ns for the emergence of a bridging cavity.[51]

D. Principal component analysis of capillary drying

Principal component analysis (PCA)[88] is a linear dimensionality reduction technique that seeks to identify, within a high-dimensional data set, a low-dimensional affine subspace within which the bulk of the variance in the data is contained. In brief, this approach identifies an ordered set of orthogonal vectors—the principal components (PCs)—each of which describes the direction along which the data exhibits maximum variance, subject to the constraint that this direction remain orthogonal to all preceding principal components. The number of PCs which should be retained is typically determined by a gap in the singular value spectrum (when such a gap is observed). For a more detailed exposition of the applications of this technique to molecular simulation, we refer the reader to standard references.[89–91]

A generic difficulty in applying dimensionality reduction techniques such as PCA to molecular simulation data arises when the simulation consists of N identical molecules, and thus a particular configuration of the system has $N!$ identical states formed by simply swapping the identities of the molecules. Blind application of PCA to simulation trajectories tracking the location of each molecule cannot account for this molecular "fungibility" or "democracy",[92] and therefore typically fails to identify a low-dimensional description of the system state space. In our analysis of the bilayer ice sublimation transition, this issue is further exacerbated by a variable number of molecules in the gap region as drying progresses. We tackled this difficulty by discretizing the gap region into a cubic mesh based on the geometry of the hexagonal cristobalite grid. As illustrated in Fig. 1(d), we divided the gap region into cuboidal cells possessing y and z dimensions of $\Delta y = 0.495$ nm and $\Delta z = 0.429$ nm, and spanning the gap in the x dimension, to generate a $(1\times6\times7)$ mesh. A coarse-grained description of each snapshot in each drying trajectory was synthesized by assigning the water molecules in the gap region to the cell in which the O atom was located. Each snapshot was therefore translated into a 42 element *occupancy vector* describing the integer occupation number of each cuboidal cell. Due to the different number of cells in the y and z dimensions of the cuboidal grid, and structural differences between the two edges of the plates spanning the y-dimension (cf. Fig. 1(d)), our system does not possess any strict rotational symmetries. Accordingly, we are not at liberty to buttress our data by exploiting symmetries within the system to synthesize additional symmetrized trajectories from our simulations.[93,94]

Since the occupancy of each cell was observed to rapidly fluctuate as water molecules moved across its boundaries, we elected to further abstract this description into what we shall term a *binary occupancy vector* with elements equal to 1 if the cell is occupied by any number of water molecules, and 0 if it is completely unoccupied. Although this final abstraction resulted in loss of information on the precise population of each cell within the gap, it provided a less highly fluctuating description of the system while preserving the essential feature of interest, namely whether a particular gap region is wet (1) or dry (0).

The PCs of the ensemble of binary occupancy vectors extracted from all drying trajectories provide an alternative basis set in which to describe the state of the system. Indeed, since they are computed by diagonalization of the covariance matrix, the PCs may be regarded as the "eigenbubbles" of the drying process.[95] Accordingly, an n-dimensional binary occupancy vector, $\vec{v}$, may be *exactly* represented in the PC basis as a linear combination of the n PC vectors, $\vec{PC}_i$, ordered by

decreasing singular values, and the mean binary occupancy vector, $\vec{v}_{mean}$,

$$\vec{v} = \vec{v}_{mean} + \sum_{i=1}^{n} (\vec{v}.\vec{PC}_i)\vec{PC}_i = \vec{v}_{mean} + \sum_{i=1}^{n} \alpha_i \vec{PC}_i, \quad (1)$$

where α_i denotes the projection of $\vec{v}$ into $\vec{PC}_i$.

The vector $\vec{v}$ may be *approximately* reconstructed by summing over only the top $m < n$ PCs possessing the largest singular values, where the value of m is generally motivated by a spectral gap in the singular value spectrum. These top m PCs represent a sparse basis set furnishing a lower dimensional representation of the system.[90,96] Embedding the drying trajectories into the low-dimensional space spanned by the top PCs provides a means to unite the individual simulations into a common framework, visualize their progression through state space, and codify the drying pathways followed by the system.

We note that the observed sublimation transitions at $d = 0.60$ nm did not exhibit density gradients in the x-direction, normal to the surface, with recession of the water molecules from a particular region within the gap occurring nearly simultaneously and uniformly across the entire gap region. This permitted us to treat the sublimation transition as an effectively two-dimensional process, and discretize the interplate region with gap-spanning cells. For larger plate separations, discretization in the dimension normal to the plates would be necessary to allow the capture of possible density gradients across the gap.

III. RESULTS AND DISCUSSION

A. Expanded *P-d* phase diagram

In Fig. 2 we present a P-d phase diagram of water confined between atomistically detailed hydrophobic plates at 298 K. This map represents an extension of the exploration of the phase behavior for this system pioneered by Giovambattista *et al.*[34] However, due to denser sampling of the phase space, extension to higher pressures, and the deployment of order of magnitude longer simulations, we report a richer and more detailed phase behavior than has previously been determined. In this section, we first characterize the various phases observed throughout the phase diagram, before concluding with some observations regarding phase transitions under confinement suggested by the expanded phase diagram. We recognize that the terms phase transition and phase boundary are only strictly applicable to macroscopic systems, but throughout this work we follow Bolhuis and Chandler's precedent and adopt this less formal terminology to refer to events on the microscopic scale.[50]

We observe good agreement of the current map with the previously published phase diagram (Ref. 34, Fig. 2), placing the $d = 0.80$ nm vapor-liquid phase boundary and the $d = 0.60$ nm extent of the bilayer ice at nearly identical pressures. Grand canonical Monte Carlo simulations of SPC water between smooth hydrophobic plates by Bratko *et al.*[38] identified drying transitions at [$P = 0.0$ GPa, $d \approx 0.79$ nm] and [$P = 0.10$ GPa, $d \approx 0.42$ nm]—where d values have been converted into the convention employed in this work[34]—in good agreement with the phase boundaries reported here for an atomistic surface.

Zangi and co-workers have conducted detailed investigations into the phase behavior of water confined between SiO_2 plates,[85] but these authors investigated plates with atoms in a triangular rather than hexagonal arrangement and employed the TIP5P model of water. Simulations of bulk water have shown that the phase behavior, and in particular the molecular structure of crystalline phases, is influenced by the choice of water potential model.[97,98] Accordingly, a quantitative comparison of the results of Zangi *et al.* with the present work would be inconclusive. We believe that a future study elucidating the commonalities and differences between the confined water phase behavior computed using different underlying water potential models would be of interest.

In Fig. 3(a) we present the P-d-σ phase diagram, where σ is the number of water molecules residing in the gap per unit plate area, and of which Fig. 2 is a two-dimensional projection. In Fig. 3(b), we present the d-σ projection of Fig. 3(a) to illustrate the interesting result that for plate separations $d \leq 0.65$ nm, σ is the sole discriminant of the confined phase behavior, irrespective of P or d, discriminating between the vapor, monolayer ice, monolayer liquid, bilayer ice, and frustrated trilayer heterogeneous fluid phases. At larger plate separations, σ ceases to be a unique classifier, with the liquid existing at the same σ values as both the bilayer ice, frustrated trilayer heterogeneous fluid, and trilayer heterogeneous fluid. That the phase map of room temperature water confined between narrowly separated hydrophobic plates ($d \leq 0.65$ nm) at pressures $P \leq 1.0$ GPa is dictated exclusively by the number of confined water molecules per unit plate area, suggests that geometric packing constraints, rather than details of the bulk pressure and gap geometry, govern the phase behavior of the confined fluid. We now discuss the various phases whose range of stability is shown in Fig. 2.

1. Vapor

By equating the grand potentials of the vapor and liquid phases of a homogeneous macroscopic continuum fluid confined between two identical square plates of side length L, the critical plate separation below which the liquid becomes metastable with respect to the vapor, d_{crit}, is related to the bulk pressure, P, as[1,35,54]

$$d_{crit} = \frac{-2\gamma_{vl}\cos\theta_c}{(P - P^*) + \frac{4\gamma_{vl}}{L}}, \quad (2)$$

where γ_{vl} is the vapor-liquid interfacial tension, P^* is the vapor pressure at the given temperature, and θ_c is the contact angle at which an equilibrium liquid/vapor interface meets the plates. Contrary to Ref. 35, we do not assume perfectly non-wetting conditions (i.e., hard-sphere walls), but rather use Young's equation[99] to arrive at the well-known expression containing the contact angle.[54] This relationship demonstrates that: (1) drying may be induced at any plate separation d by lowering the pressure such that $d_{crit} > d$ and (2) d_{crit} should be a decreasing function of pressure. For all plate separations considered, we observe a confined vapor phase at sufficiently

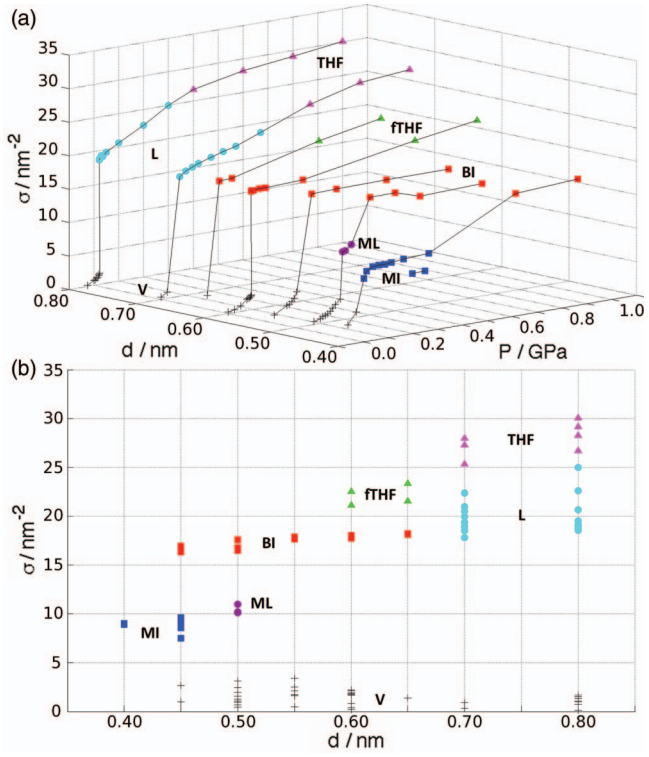

FIG. 3. (a) P-d-σ phase diagram for water confined between atomistically detailed hydrophobic plates at $T = 298$ K. σ, the number of water molecules per unit area residing within the gap, was computed by averaging over the final 2 ns of each 5 ns molecular dynamics simulation. The pairing of phases with symbols is identical to that in Fig. 2. For clarity of exposition in the σ dependence of the phase behavior, state points at which bulk cavitation or phase coexistence were observed are omitted in the present figure. Additionally, the state points at [$P = 0.50$ GPa, $d = 0.45$ nm] and [$P = 0.60$ GPa, $d = 0.45$ nm] were removed due to imperfections in the bilayer crystals which did not heal on the time scale of the simulations (cf. Sec. III A), resulting in artificially low σ values. The standard deviation in σ is less than ± 1 nm^{-2} for all state points. Points sharing common d values are connected by lines as a guide to the eye. (b) Two-dimensional projections of panel (a) into the d-σ plane illustrates that for plate separations $d \leq 0.65$ nm, σ is a unique discriminant of the phase behavior. At larger plate separations, this ceases to be true. For the monolayer and bilayer ice phases, we observe good agreement with the theoretical σ values for idealized infinite crystals of 9.15 nm^{-2} and 18.31 nm^{-2}. The dispersion around these values arises from edge effects in the finite sized plates employed in this work, and imperfections in the crystal structures.

low pressures, which, consistent with previous work,[34] constitutes an effective vacuum (Fig. 2). Further reduction in pressure leads to bulk cavitation, indicative of the thermodynamic instability of the bulk liquid at this temperature and pressure.

Whereas the analysis leading to Eq. (2) is restricted to vapor-liquid transitions (for which indeed Fig. 2 shows a simple monotonic relationship between d_{crit} and P), the complex behavior shown in Fig. 2 reflects the existence of structurally distinct confined morphologies in equilibrium with the vapor phase at different values of P, which may not be treated as a single "confined phase" with fixed thermodynamic properties. However, over ranges of d values for which the confined phase in equilibrium with the vapor does not change, d_{crit} is—to within the resolution of the data points used to construct our phase diagram—a monotonically decreasing function of P.

It should be emphasized that when L is of nanoscopic dimensions, the second term in the denominator of Eq. (2) is much larger than the first[1,35] (e.g., for water at ambient conditions $\frac{4\gamma_{vl}}{L(P-P^*)} \sim 10^3$ for $L = 1$ nm), and one has, in that case, the important limit $d_{crit} \propto L$. This relationship, in turn, should break down at small enough dimensions where a macroscopic thermodynamic treatment becomes inaccurate.[35]

Using literature values for the vapor pressure[100] and surface tension[101] of bulk water at 298 K, and the equilibrium contact angle of $\theta_c = 105°$ previously computed by Giovambattista *et al.*[102] for water on this surface at 300 K, we plot on Fig. 2 the vapor-liquid phase boundary predicted by Eq. (2) over the range of plate separations for which we observe a vapor-liquid phase transition. The predicted phase boundary possesses a slope in qualitative agreement with that calculated from our simulations, but is displaced from the observed phase boundary by approximately (-0.05) GPa, or (-0.45) nm. This quantitative discrepancy may be understood as a failure of the continuum treatment of the fluid on length scales approaching a molecular diameter.[35] Interestingly, if we treat the contact angle as an adjustable parameter, we observe relatively good agreement of the predicted and observed vapor-liquid phase boundaries for $\theta_c = 130°$ (Fig. 2). The discrepancy between the fitted (130°) and actual (105°) contact angles, and the disagreement in the slope of the observed and predicted boundaries, may be attributed to the approximation of the confined water as a continuum fluid.

2. Bilayer ice

A bilayer crystalline phase is observed over a large range of plate separations and pressures (Fig. 2) and is identical to that previously reported in this system by Giovambattista *et al.*,[34] and similar to that observed for TIP4P water in a slit nanopore with smooth hydrophobic walls by Koga *et al.*[103,104] In simulations employing infinite plates, Giovambattista *et al.*[75] and Johnston *et al.*[42] reported continuous bilayer ices possessing long range crystalline order. The bilayer character of this phase is apparent from the bimodality of $P_{O,\,gap}(x)$ in Fig. 4 for a representative simulation of this phase at [$P = 0.20$ GPa, $d = 0.55$ nm]. The vanishing probability density extending ± 0.05 nm from the midplane is attributable to the crystalline nature of this phase suppressing exchange of water molecules between the two layers. The measured self-diffusivity across the bilayer of D $\approx 1 \times 10^{-9}$ cm^2/s (Fig. 6) is four orders of magnitude less than that of bulk liquid water at standard temperature and pressure (D $\approx 2.2 \times 10^{-5}$ cm^2/s), but an order of magnitude larger than for normal (I_h) ice (D $\approx 1 \times 10^{-10}$ cm^2/s).[105]

The atomic details of the walls (Fig. 1(d)) impose hexagonal ordering onto each layer of the in-registry bilayer, resulting in an intra-layer nearest neighbor O-O distance of ~0.29 nm, which closely matches the nearest neighbor distance in bulk water of 0.28 nm.[106] Furthermore, the nearest neighbor distance *between* bilayers is also ~0.29 nm,[34] permitting propagation of the hydrogen bonding network both within and between layers. From simple geometric analysis of the hexagonal crystal,[34] the second nearest neighbor intra-layer O-O

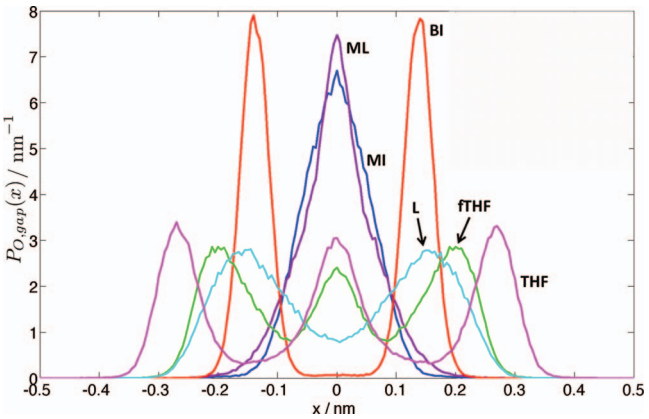

FIG. 4. $P_{O,\,gap}(x)$, for each of the six "wet" confined morphologies. In this, and the following two figures, calculations for each phase were conducted at the boxed state points in the phase diagram presented in Fig. 2, and we follow the pairing of colors and phases adopted therein: L—liquid [$P = 0.20$ GPa, $d = 0.70$ nm], ML—monolayer liquid [$P = 0.20$ GPa, $d = 0.50$ nm], BI—bilayer ice [$P = 0.20$ GPa, $d = 0.55$ nm], MI—monolayer ice [$P = 0.20$ GPa, $d = 0.45$ nm], THF—trilayer heterogeneous fluid [$P = 0.60$ GPa, $d = 0.80$ nm], and fTHF—frustrated trilayer heterogeneous fluid [$P = 0.75$ GPa, $d = 0.65$ nm]. $x = 0$ nm is defined as the location of y,z-mid-plane lying equidistant between the plates. Normalization of $P_{O,\,gap}(x)$ by the area of the plates, $A = (3.218 \times 3.215)$ nm$^2 = 10.35$ nm^2, yields the local density profile across the gap, $\rho_{O,\,gap}(x)$.

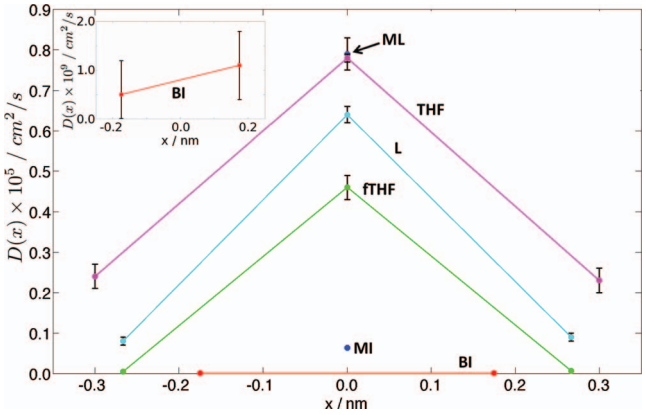

FIG. 6. Self-diffusivity as a function of transverse gap position, $D(x)$, for each of the six "wet" confined phases computed at the boxed state points in the phase diagram in Fig. 2. For each phase, the gap region was partitioned into a number of slices of equal width commensurate with the number of lateral layers in the phase and is reflected in the number of points in each curve. The approximate symmetry of the curves around $x = 0$ nm arises due to the mirror symmetry of the system around the mid-plane of the gap. Uncertainties were computed from the standard deviation in the self-diffusivity computed over the five 4 ns blocks of the full 20 ns trajectory. Where error bars are not visible, the uncertainty is smaller than the symbol size. The inset provides a zoomed in view of the bilayer ice self-diffusivity profile.

distance is ~0.49 nm ($\sqrt{3} \times 0.29$ nm), and the third nearest neighbor is ~0.73 nm (2.5×0.29 nm). The corresponding second and third nearest neighbor inter-layer distances *between* bilayers are ~0.41 nm ($\sqrt{2 \times 0.29^2}$ nm) and ~0.58 nm ($\sqrt{0.29^2 + (\sqrt{3} \times 0.29)^2}$ nm). All of these peaks are visible in the rdf in Fig. 5. The absence of the peaks at ~0.41 nm and ~0.58 nm in all other morphologies investigated—with the exception of the trilayer heterogeneous fluid—is indicative of the absence of correlations between adjacent layers of water.[85]

The formation of the bilayer ice at the state points [$P = 0.50$–1.0 GPa, $d = 0.45$ nm] proceeds by the formation of a metastable monolayer ice (described below), which then transforms to the equilibrium bilayer on a nanosecond time scale. The nanosecond time scale required for the formation of this phase suggests that simulations shorter than several nanoseconds are insufficient to fully explore the equilibrium phase behavior of water confined between nanoscopic hydrophobic plates. The severe geometric restrictions imposed by the geometry of the gap retard the adoption of the bilayer morphology and renders the crystal highly susceptible to defect formation, whereby islands of the monolayer ice become surrounded by bilayer crystal. The very low mobility of molecules in the bilayer phase (Fig. 6) makes the healing of these defects by the influx of additional water molecules a slow process that does not fully complete on a nanosecond time scale. For larger plates, it is likely that these defects will be kinetically trapped into the crystal on relatively very long time scales.

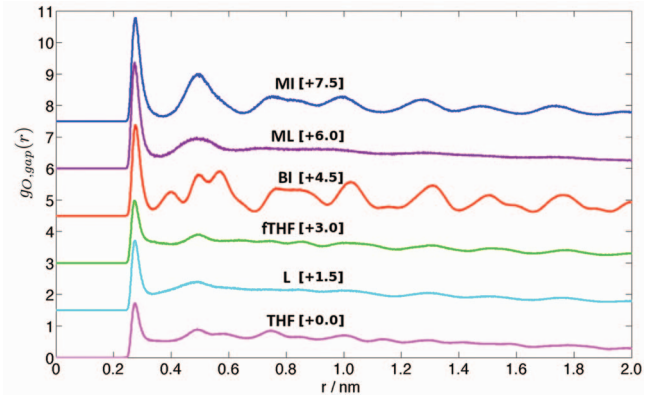

FIG. 5. $g_{O,\,gap}(r)$, for each of the six "wet" confined morphologies computed at the boxed state points in the phase diagram in Fig. 2. r is the Euclidean distance between O atom centers. Normalization of $g_{O,\,gap}(r)$ is performed with respect to a cylindrical volume of radius r and height equal to the gap width, d. For clarity of presentation, each curve is shifted vertically by the value indicated in square brackets.

3. Liquid

At plate separations $d \geq 0.7$ nm, and $P \approx 0.0$–0.40 GPa, we observe the existence of a liquid phase (Fig. 2). Analysis of the simulation conducted at [$P = 0.20$ GPa, $d = 0.70$ nm] shows a clear bimodality in $P_{O,\,gap}(x)$, with the peaks located symmetrically around the mid-plane and proximate to the walls (Fig. 4). In contrast to the bilayer ice phase, significant probability density resides between the peaks, indicating that water molecules populate the entire gap region and are not restricted to lie exclusively within one of the two bilayers. This interpretation is consistent with visual inspection of snapshots transverse to the gap, which exhibit a gross bilayer structure but clearly reveal the presence of significant

numbers of molecules located interstitially between these layers (Fig. S1 in the supplementary material[107]).

As for the monolayer liquid, peaks in the rdf are observed at ∼0.29 nm and ∼0.49 nm (Fig. 5) corresponding to the nearest, and second nearest *intra*-layer neighbors. The absence of a third nearest neighbor peak at ∼0.73 nm is indicative of the absence of long range order. This stands in contrast to the trilayer heterogeneous fluid (THF) (described below), where the two outer layers adopt crystalline configurations.

The self-diffusivity of the liquid at the mid-plane of the gap is $D \approx 6.4\times10^{-6}$ cm^2/s (Fig. 6), about 30% of the bulk ambient liquid value ($D \approx 2.2\times10^{-5}$ cm^2/s).[105] Nearer the walls, the diffusivity drops approximately eightfold to $D \approx 8.5\times10^{-7}$ cm^2/s, reflecting the lower mobility of the outer layers of water proximate to the plate surfaces.

Contrary to simulations conducted by Zangi and coworkers, we do not observe the appearance of a second bilayer liquid upon reducing the gap width below that at which the bilayer ice is observed,[85] but rather see the appearance of monolayer liquid and ice morphologies. This discrepancy may be attributable to our use of SPC/E water and in-registry plates with hexagonally arranged wall atoms, compared to the use of TIP5P water with out-of-registry plates and wall atoms in a triangular arrangement in the work by Zangi *et al.*[85]

4. Monolayer liquid

Over a small region of the phase diagram (Fig. 2), we observe a monolayer liquid similar to that reported by Zangi and co-workers for TIP5P water confined between cristobalite walls at ∼0.50 nm plate separations.[85] We term this phase a "structured" monolayer liquid due to the influence of the walls in templating quasi-hexagonal structure into the liquid, inducing a semi-ordered patterning reminiscent of the crystal structure of the monolayer and bilayer ices (Fig. S2[107]). This wall influence results in enhanced short-ranged order, evinced in a nearest neighbor peak in the rdf approximately 15% higher than that in bulk SPC/E water (Fig. 5).[76] The absence of long ranged order in the rdf, together with the high mobility of the molecules in this phase, however, distinguish the monolayer liquid from the monolayer ice described below.

The self-diffusivity of monolayer liquid of $D \approx 7.9 \times 10^{-6}$ cm^2/s (Fig. 6) is, remarkably, the highest of all six of the boxed state points investigated in Fig. 2, 20% higher than the mid-plane of the liquid, although still almost three times lower than that of bulk liquid water at standard temperature and pressure ($D \approx 2.2 \times 10^{-5}$ cm^2/s).[105] The absence of inter-layer hydrogen bonds evidently imparts significant additional translational and rotational freedom to the molecules in this phase compared to the multilayer phase, but is countered by the severe geometric restrictions to relative motion imposed by confinement within such a narrow gap. The diffusivities of monolayers of TIP5P water between cristobalite walls reported by Zangi ($D \approx 4\times10^{-5}$ cm^2/s),[85] and TIP3P water between (6,6) carbon nanotube membranes reported by Kalra *et al.*[108] ($D \approx 2\times10^{-5}$ cm^2/s), are approximately 2–5 times greater than the values calculated in this work, illustrating the sensitivity of these results to the precise details of the system, and geometry of the gap.[34]

5. Trilayer heterogeneous fluid

In large gaps ($d \geq 0.70$ nm) at high pressure ($P \gtrsim 0.45$ GPa) we observe the THF previously reported by Giovambattista *et al.*[75] This phase is characterized by a monolayer of disordered liquid sandwiched between two crystalline-ordered layers at the walls that possess the same hexagonal templated structure as the bilayer ice. The trilayer character is apparent from the $P_{O,\,gap}(x)$ curves in Fig. 4. The self-diffusivity of the central liquid layer is nearly identical to that of the monolayer liquid phase ($D \approx 7.8\times10^{-6}$ cm^2/s), but only approximately fourfold higher than that of the crystalline-ordered layers at the wall (Fig. 6). We attribute this rather high lateral mobility of the ordered layer at the wall to the capacity for molecular exchange with the disordered liquid layer. Plan and transverse snapshots of this phase are presented in Fig. S3.[107]

$P_{O,\,gap}(x)$ reveals that, as was the case for the bilayer ice, the separation between adjacent layers of the THF is equal to the intra-layer nearest neighbor distance of ∼0.29 nm. The peak in the rdf in Fig. 5 at this distance is therefore composed of both inter and intra layer correlations. Since the central layer is a disordered liquid, the peak at ∼0.58 nm is attributable to the separation of the in-registry hexagonal lattices in the outer layers, rather than third nearest neighbor correlations between adjacent layers as was the case for the bilayer ice. Finally, the ∼0.49 nm peak corresponds to second nearest *intra*-layer neighbors.

6. Frustrated trilayer heterogeneous fluid (fTHF)

At slightly narrower plate separations than those at which we observed the trilayer heterogeneous fluid ($d \approx$ 0.60–0.65 nm), we report the existence of a morphology similar to the THF that we term the frustrated trilayer heterogeneous fluid. As for the THF, this phase contains three distinct layers, but as evinced in Fig. 4, the layers are less distinct than in the case of the THF, with significantly higher probability density, $P_{O,\,gap}(x)$, in the regions between the peaks. Snapshots of the three layers illustrate that the two outer layers of the fTHF have crystalline order, with morphologies similar to those observed for the THF (cf. Figs. S4(a) and S4(c), and S3(a) and S3(c)[107]). Conversely, the central liquid layer is markedly less dense in the fTHF than the THF (cf. Figs. S4(b) and S3(b)[107]), with the steric constraints imposed by the narrowness of the gap requiring the molecules comprising this layer to reside in the pockets formed between the centers of the in-registry hexagons of the upper and lower layers. The large separation between O atoms residing in adjacent pockets within the central layer (∼0.495 nm) precludes the formation of an intra-layer hydrogen bonding network,[109] resulting in the formation of bonds between molecules residing in the central layer with those of the two outer layers (Fig. S4(d)[107]). The increased inter-layer interactions in the fTHF compared to the THF, coupled with the tighter geometry of the gap, is correlated with the observation of more frequent molecular

exchanges between the layers, leading to elevated probability densities in the inter-layer regions (Fig. 4), disruption of the hexagonal crystal structure of the outer layers (Fig. S4(a) and S4(c)[107]), and less long range order (Fig. 5) in the fTHF compared to the THF morphology.

The self-diffusivity of the molecules in each layer of the fTHF is significantly depressed compared to that of the THF (Fig. 6). Although it is difficult to deconvolute the combined effects of the narrower gap and change in structural morphology, we observe that the self-diffusivity of the central liquid layer is $D \approx 4.6\times10^{-6}$ cm^2/s, approximately half that of the central THF layer and the monolayer liquid. We emphasize that the boundary between the THF and fTHF phases is ill defined, and our discrimination between the two phases somewhat qualitative. With the available data, we cannot discard the possibility that the THF and fTHF are smoothly connected (e.g., upon increasing d at constant P) and that they may form a single phase. Additional simulation and characterization would be required for a more detailed investigation of the boundary region. In addition to purely structural metrics, we suggest that comparison of the self-diffusivity of the central layer to that of the monolayer liquid, the existence of a spanning intra-layer hydrogen bonding network within this layer, or tracking the heat capacity across the putative transition may be useful measures by which to better define the phase boundary.

The phase boundary between the fTHF and the bilayer ice is the only region on the phase diagram at which we observe equilibrium phase coexistence (Fig. 2). (As discussed below, the solid-vapor coexistence at [$P \leq 0.15$ GPa, $d = 0.40$ nm] appears to be the result of kinetic arrest.) Simulations at the three state points along this phase boundary—[$P = 0.30$ GPa, $d = 0.65$ nm], [$P = 0.50$ GPa, $d = 0.60$ nm] and [$P = 1.0$ GPa, $d = 0.55$ nm]—exhibit periodic ingress of bulk water molecules into the mid-plane of the gap between the two planes of the crystalline bilayer. These molecules occupy interstitial sites between the hexagons constituting the crystal bilayer and induce local melting into a trilayered structure resembling the fTHF (Fig. S5[107]). We suggest that the free energy barrier between these two phases may be sufficiently low to permit the transitions between these phases and the observation of coexistence on the time and length scales of our simulations.

Finally, we propose that it may be of interest to explore whether the fTHF morphology is supported by out-of-registry plates such as those considered by Zangi and co-workers,[85] where the crystalline arrangements of the upper and lower layers are expected to be misaligned, eliminating the sterically open pockets within which the molecules of the central layer reside.

7. Monolayer ice

At $d = 0.45$ nm over the pressure range $P \approx 0.15$–0.45 GPa we observe a monolayer crystalline phase with a wall-templated hexagonal structure similar to that exhibited by the bilayer ice (Fig. 2). $P_{O,\,gap}(x)$ in Fig. 4 illustrates that the oxygen atoms of the water molecules constituting the monolayer follow a unimodal distribution centered around the mid-plane of the gap, indicative of a single planar layer. Inspection of the rdf in Fig. 5 illustrates that the monolayer phase exhibits the same peaks at 0.29, 0.49, and 0.73 nm as those *intra*-layer peaks computed by geometrical considerations for the bilayer ice morphology. Conversely, the second and third nearest neighbor *inter*-layer peaks exhibited by the bilayer at 0.41 and 0.58 nm are not observed. This peak signature indicates that the hexagonal organization of the O atoms of the monolayer ice is very similar to a single layer of the bilayer ice, but as we explore below, the arrangement of the H atoms, and by extension the hydrogen bonding network, is markedly different. Nevertheless, the structural similarity of the monolayer ice to a single layer of the bilayer morphology suggests that this phase may also support the long range crystalline order previously reported in the bilayer ice.[42,75]

The self-diffusivity of the monolayer ice, $D \approx 6.3 \times 10^{-7}$ cm^2/s (Fig. 6), is in excess of two orders of magnitude greater than that of the bilayer ice, but more than an order of magnitude smaller than that of the monolayer liquid or bulk liquid water.[105] In the bilayer crystal, the constituent water molecules obey the bulk ice rule[110] whereby each water molecule is a double donor and double acceptor of hydrogen bonds. In contrast, the narrow $d = 0.45$ nm plate separation at which we observe the monolayer ice restricts the hydrogen bonding network to a plane, allowing each water molecule to participate in only three hydrogen bonds. The electrostatically neutral, hydrophobic walls preclude hydrogen bonds perpendicular to the plane, and the exclusively dispersive wall interactions permit significant mobility of the water molecules in the transverse direction. This is apparent in the larger $P_{O,\,gap}(x)$ peak width (Fig. 4) and self-diffusivity (Fig. 6) of the monolayer ice compared to the bilayer crystal. Upon widening the gap by only 0.05 nm, to 0.50 nm, the monolayer ice spontaneously melts into the lower free energy monolayer liquid (Fig. 2), where the energetic stabilization of the weak in-plane hydrogen bonding network is outweighed by a compensatory entropy gain associated with transition to a fluid phase in the larger confining volume.

Zangi and Mark[111] previously reported a buckled ice monolayer in molecular dynamics simulations of TIP5P[112] water confined between two atomistically detailed SiO_2 quartz plates with triangularly arranged atoms. The same phase was subsequently observed between smooth walls in simulations by Kumar *et al.*,[14] and Koga and Tanaka.[113] Spagnoli *et al.*[114] employed atomic force microscopy to image ice monolayers upon an exposed mica surface, which appear to exist in a buckled film arrangement consistent with this structure. Very recently, Bai *et al.* reported a novel monolayer crystalline phase of TIP5P water confined between both atomistically detailed and smooth hydrophobic walls.[43] The structure of the planar crystal possesses an Archimedean 4×8^2 truncated square geometry, previously reported by Yang *et al.* in simulations of a water monolayer adsorbed to a β-cristobalite (1.0.0) surface,[115] in which space is tiled by interlocking squares and octagons. Interestingly, Bai *et al.* also report coexistence between the Archimedean and the buckled monolayer morphologies.[43]

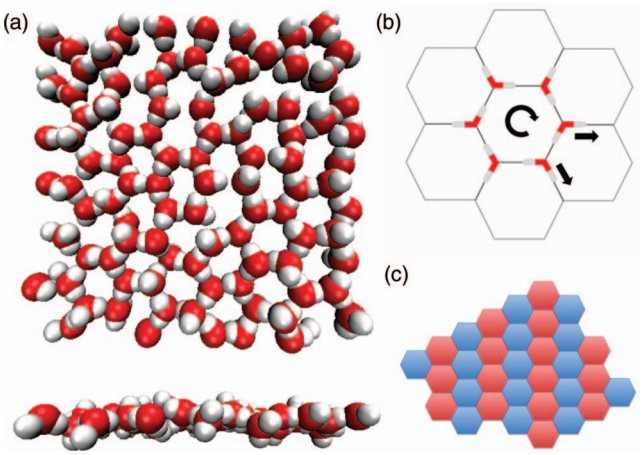

FIG. 7. Geometry of the monolayer ice. (a) Plan and transverse snapshots of the monolayer ice phase at [$P = 0.20$ GPa, $d = 0.45$ nm]. The field of view has been restricted to $(-0.25) < x \leq 0.25$ nm in the x-direction to permit visualization of the inter-plate region. Templating by the walls imparts a hexagonal structure inducing an arrangement of O atoms resembling that of both a single sheet of the bilayer ice and the theoretical structure of a non-dissociated monolayer of water adsorbed onto a Ru(0001) surface.[116,117] (b) Since this morphology resides in the plane, satisfaction of all hydrogen bonds is forbidden, prohibiting adherence to the bulk ice rules.[110] A simple geometric proof by contradiction of this argument proceeds by assuming that all donor-acceptor pairs are satisfied, which requires that all hydrogen bond around the circumference of a single hexagon point in the same direction, as illustrated in the central cell of this schematic. The inconsistency arises from the imposition upon all adjacent hexagons a configuration of three hydrogen bonds in which two point in one direction and the third in the other. (c) Geometric arguments dictate that at least one defect (unsatisfied hydrogen bond) must exist per hexagonal cell. The number of defects is minimized in an arrangement in which the orientation of hydrogen bond vectors alternates between clockwise (red) and counter-clockwise (blue) along two axes of the hexagonal tiling, generating alternating stripes of a single orientation in the third axis. Defects occur where hexagons of the same color share an edge.

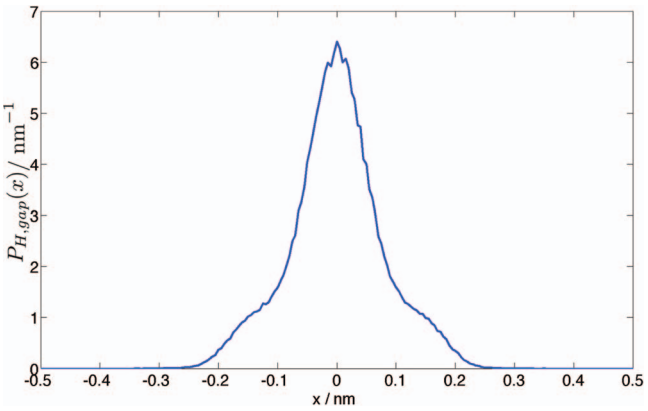

FIG. 8. Probability density function for the observation of either H atom of a confined water molecule as a function of the transverse distance across the gap, $P_{H,\,gap}(x)$, for monolayer ice phase observed at state point [$P = 0.20$ GPa, $d = 0.45$ nm]. Normalization by the area of the plates, $A = (3.218 \times 3.215)$ nm^2 $= 10.35$ nm^2 yields the local density profile across the gap, $\rho_{H,\,gap}(x)$.

In the current work, we report a novel monolayer ice distinct from either of these two geometries. The O atoms of the constituent water molecules reside in a single plane (Figs. 4 and 7(a))—as opposed to the two distinct layers of the buckled monolayer (cf. Fig. 3(b) in Ref. [111])—and tile space in a regular hexagonal geometry. The strong templating effect of the in-registry, hexagonally arranged walls on the monolayer ice morphology leads us to speculate that its absence in the simulations of Zangi and Mark may be attributable to the out-of-registry, triangularly arranged plates.[111] Interestingly, the area density of the hexagonal monolayer and the Archimedean morphology are nearly identical at ~ 9 nm^{-2}, although the former was observed at [$T = 298$ K, $P \approx 0.2$ GPa] and the latter at [$T = 250$ K, $P \approx 0$ GPa].[43] To the best of our knowledge, the in-plane hexagonal monolayer ice we observe has not been previously reported, and we proceed to more fully characterize it by analysis of the H atom configuration and hydrogen bonding network.

Similar to $P_{O,\,gap}(x)$ (Fig. 4), the pdf of the H atom positions across the gap, $P_{H,\,gap}(x)$, in Fig. 8 is unimodal and centered at $x = 0$ nm, indicating that the highest density of inter-plate water H atoms is located in the same plane as the O atoms, consistent with a two-dimensional, in-plane hydrogen bonding network. Unlike $P_{O,\,gap}(x)$, however, $P_{H,\,gap}(x)$ possesses two "wings" corresponding to an elevated probability of observing H atoms away from the mid-plane. The simulation snapshot of the monolayer ice in Fig. 7(a) illustrates the hexagonal arrangement of water molecules, each of which participates in three in-plane hydrogen bonds, acting either as a double donor and single acceptor, or double acceptor and single donor. Conversely, in the buckled monolayer[111] each molecule obeys the bulk ice rule[110] rule, acting as a double donor and double acceptor. Bai *et al.* suggest that the planar Archimedean tiling also obeys the bulk ice rule, by virtue of specific molecules in the arrangement acting as "double donors to a single acceptor" in which both O-H vectors are obliquely oriented towards a single neighboring O atom.[43]

The planar monolayer morphology is frustrated in that there is no way to arrange the hydrogen bonds in a plane-filling hexagonal tiling such that all H atoms participate in a donor-acceptor pair, as is easily demonstrated by the following argument. For all of the O-H vectors forming the edges of a single hexagon of water molecules in Fig. 7(a) to participate in hydrogen bonds, all vectors must point in a clockwise (or equivalently, anticlockwise) direction, as illustrated in Fig. 7(b). The O-H vectors radiating out from this central hexagon form edges in adjacent hexagons, which, by the same argument, must contain O-H bonds all pointing in the same direction in order for them to participate in a donor-acceptor pair. Here we encounter an inconsistency, since each pair of neighboring radiating O-H vectors that form edges of an adjacent hexagon point in opposing directions, as illustrated for one such pair in Fig. 7(b). This necessarily leads to the existence of "defects" at which two O-H vectors overlap, and steric constraints forbid both from participating as hydrogen bond donors. (As explained in the next paragraph, we term this arrangement a defect since it results in one O-H vector rotating to point out of the plane of the monolayer ice, resulting in a dangling hydrogen bond.) Extending this argument to a tiling of the plane, we encounter defects where hexagons of the same "directionality" share an edge. Building

on this geometric argument, in Fig. 7(c) we illustrate the tiling of hexagon directionalities that minimizes the number of defects, corresponding to one per hexagon. Discounting finite size and edge effects, for the 33 complete hexagons formed between the plates in our simulated system (Fig. 7(a)), this arrangement of anticlockwise and clockwise hexagon directionalities would be expected to contain defects in 33 of the 121 edges (~27%).

To investigate the behavior of the O-H vectors in response to defects, we computed pdfs in the angle of inclination from the y, z-plane, θ_1 and θ_2, of the inter-plate water molecule O-H vectors, O-H_1 and O-H_2. We employ the convention that $\theta = 90^\circ$ if the O-H vector is pointing directly towards the upper wall, $(-90)^\circ$ if it is oriented towards the lower wall, and 0° if it is lying in the y,z-plane. In Fig. 9(a) we present a one-dimensional pdf, $P_{\vec{OH},gap}(\theta)$, produced by averaging over θ_1 and θ_2. The distribution is symmetric due to the indistinguishability of the top and bottom walls, and is peaked at $\theta = 0^\circ$, where the O-H vectors lie in the same plane as the O atoms and participate in the two-dimensional hydrogen bonding network. The local maxima in $P_{\vec{OH},gap}(\theta)$ at approximately $\pm 70^\circ$ correspond to the wings of the $P_{H,\,gap}(x)$ distribution in Fig. 8, where there is an elevated probability of finding H atoms away from the mid-plane. The location of these maxima is consistent with the O-H_1 vector of a particular water molecule lying in the y,z-plane and the O-H_2 vector (or vice versa) rotated 90° out of the plane. In this configuration, $\theta_1 = 0^\circ$, and with an H-O-H angle in the SPC/E model of 109.47°, $\theta_2 = (180 - 109.47)^\circ \approx 70.5^\circ$. This suggests that when two O-H vectors overlap in a defect, the system responds by rotating one vector 90° out of the plane, permitting the other to establish a well-formed hydrogen bond. Visual confirmation of this behavior is apparent in Fig. 7(a), and further supported in our analysis of $P_{\vec{OH},gap}(\theta_1, \theta_2)$ in Fig. 9(b). Adopting $\theta = \pm 30^\circ$ as a geometric cutoff for the existence of an in-plane hydrogen bond,[109] integration of the wings of the pdf in Fig. 9(a) reveals the percentage of unsatisfied hydrogen bond donors to be $P_{\vec{OH},gap}(|\theta| \geq 30^\circ) \approx 33.3\%$, in good agreement with the value of ~27% predicted from geometric considerations (cf. Fig. 7(c)).

In Fig. 9(b) we present the two-dimensional analog of Fig. 9(a), where histograms were collected in the $[\theta_1, \theta_2]$ over the inter-plate water molecules. For clarity of representation, we have elected to transform the two-dimensional probability distribution, $P_{\vec{OH},gap}(\theta_1, \theta_2)$, into a free energy surface (FES) using the standard statistical mechanical relationship between probability density and free energy in the *NPT* ensemble, $\beta G_{\vec{OH},gap}(\theta_1, \theta_2) = -ln[P_{\vec{OH},gap}(\theta_1, \theta_2)\ \Delta\theta_1 \Delta\theta_2]$, where G is the Gibbs free energy and $\beta = 1/k_B T$, where k_B is Boltzmann's constant and T the absolute temperature. This landscape may therefore be interpreted as the FES experienced by each individual water molecule residing within the monolayer ice, parametrized by the angles of inclination of each of its two O-H vectors, in a mean field approximation. The global minimum (corresponding to the probability maximum) at $[\theta_1 = 0^\circ, \theta_2 = 0^\circ]$ corresponds to a molecule with both O-H vectors lying in the y,z-plane, presumably participating as hydrogen bond donors. The four local minima in the vicinity of $[\theta_1 = \pm 80^\circ, \theta_2 = \mp 20^\circ]$ and $[\theta_1 = \pm 20^\circ, \theta_2 = \mp 80^\circ]$ correspond to one O-H vector lying nearly in the plane, participating in the planar hydrogen bonding network, and the other rotated 90° around this vector, presumably to move out of the plane to resolve the steric clash arising from the presence of a defect. (Collapsing the two-dimensional landscape to a one-dimensional curve by averaging over θ_1 and θ_2 places these local minima at $\theta = \pm 70^\circ$, as observed in Fig. 9(a).) The strong local maxima at $[\theta_1 = \pm 35^\circ, \theta_2 = \pm 35^\circ]$ correspond to both O-H vectors inclined out of the plane and pointing towards the same wall, while the broad, weak maxima at $[\theta_1 = \pm 40^\circ, \theta_2 = \mp 40^\circ]$ are associated with the vectors pointing at opposite walls. These configurations reflect the energetic destabilization associated with orientations in which neither O-H vector is engaged as an efficient hydrogen bond donor. We note that the latter orientation is reminiscent of the "double donor to a single acceptor" arrangements reported in the Archimedean tiling of Bai *et al.*, but at the higher temperatures and pressures of the current work, we find them to be

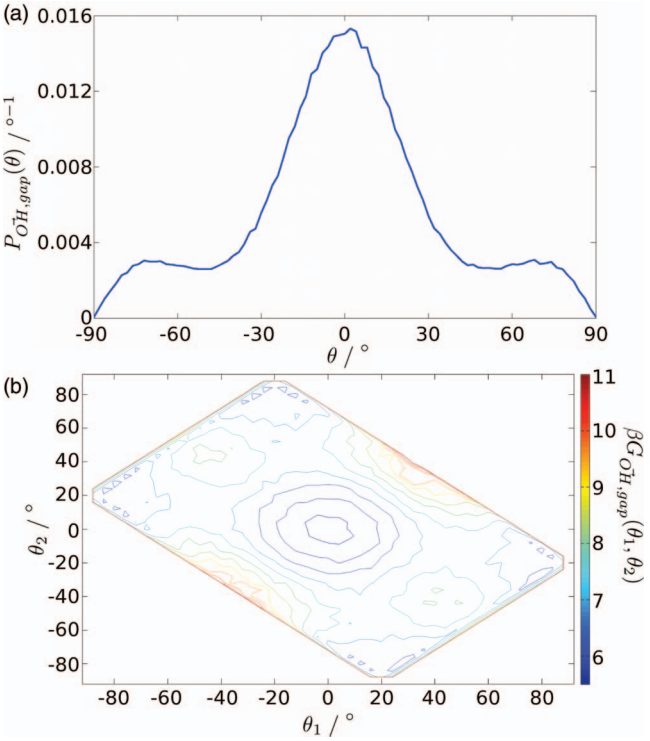

FIG. 9. Distribution of O-H vector angles of inclination in the monolayer ice. (a) Probability density function of the O-H vector angle of inclination, θ, with respect to the plane of the gap, averaged over the two O-H vectors of each water molecule residing within the gap, $P_{\vec{OH},gap}(\theta)$. We adopt the convention in which $\theta = 90^\circ$ for an O-H vector pointing towards the upper plate, $(-90)^\circ$ for those pointing towards the lower plate, and 0° for those vectors residing within the y,z-plane. The approximate symmetry around $\theta = 0^\circ$ arises from the mirror symmetry of the system around the mid-plane of the gap. (b) Mean field FES experienced by a particular water molecule residing within the monolayer ice, parametrized by the O-H angles of inclination of its O-H_1 and O-H_2 vectors, $\beta G_{\vec{OH},gap}(\theta_1, \theta_2) = -ln[P_{\vec{OH},gap}(\theta_1, \theta_2)\ \Delta\theta_1 \Delta\theta_2]$, where G is the Gibbs free energy, $\beta = 1/k_B T$, k_B is Boltzmann's constant and T the absolute temperature. The plots in both panels were computed by compiling histograms over the final 4 ns of the equilibrium simulation trajectory at the state point [$P = 0.20$ GPa, $d = 0.45$ nm], employing a bin size of $\Delta\theta = 2^\circ$ in (a), and $\Delta\theta_1 = \Delta\theta_2 = 4^\circ$ in (b). The edges of the landscape in (b) appear blunted due to the cubic grid employed in compiling the histograms.

unstable with respect to configurations possessing a single in-plane hydrogen bond. The sharp edges of the plot correspond to vanishing probability density associated with regions of $[\theta_1, \theta_2]$ phase space geometrically forbidden by the rigid 109.47° H-O-H angle in the SPC/E model.[76]

Interestingly, the observed morphology of the monolayer ice closely resembles the theoretical structure of a non-dissociated monolayer of water adsorbed onto a Ru(0001) surface.[116,117] Controversy still surrounds the precise geometry and degree of dissociation of the monolayer, but current experimental and theoretical results suggest that it forms a relatively planar structure.[116,118] Feibelman and Alavi noted that every pair of neighboring water molecules in the structure donates three hydrogen bonds, with the fourth pointing upwards into the vacuum or down towards the surface.[119] Following Pauling's celebrated approach to the calculation of the residual entropy of ice I_h, the authors computed the residual entropy of the monolayer structure to be almost twice that of bulk ice.[119,120] In the context of the current work, the residual disorder in the hydrogen bond orientations contributes an entropic stabilization of the confined monolayer ice.

Similar to Ref. 34, we find that for $d < 0.40$ nm interplate water molecules are sterically immobilized between the surfaces. At $d = 0.40$ nm, water molecules in the gap are mobile, but their mobility is greatly retarded due to the steric hindrances of the plates. At such small plate separations, water molecules are only able to fit into the interstices between the opposing silanol O atoms protruding from the SiO_2 surfaces, and their motion seems to proceed by an activated hopping process between neighboring sites (Fig. S6[107]). These interesting kinetics may be amenable to modeling as a 2D random walk, similar to the 1D model developed for single file water transport through a carbon nanotube by Kalra *et al.*[121]

For $[P \leq 0.15$ GPa, $d = 0.40$ nm], we observe solid-vapor coexistence between an island of the monolayer ice in the center of the plates, separated from the bulk liquid by a halo of vapor (Fig. S6[107]). Due to the low mobility of the interplate water molecules for such narrow plate separations, the ice cluster appears to be a kinetically arrested structure, and this coexistence is speculated to be only metastable on the nanosecond time scale of the simulations. Accordingly, we have indicated the observed coexistence by superimposing symbols for both the monolayer ice and vapor phases on the phase diagram in Fig. 2, but have not continued the schematic phase boundary into this region.

8. Phase transitions

The phase diagram constructed in Fig. 2 permits the interpretation of an experimentally observed phase transition, and also hints at the existence of some intriguing phase behavior. In a study of water confined between mercury hemispheres at 265 K, Porter and Zinn-Warner measured the Young's modulus of the confined phase to report a bilayer ice at gap widths of approximately 0.50 nm, which transitioned to a multilayer fluid at separations of 0.60–0.80 nm.[122] Precise interpretation of these results in the context of our phase diagram is precluded by differences in temperature and plate geometry and structure, but we propose that the multilayer fluid may correspond to the confined liquid phase we observe in our simulations. On the phase diagram presented in Fig. 2, this transition would correspond to an isobaric transition across the bilayer ice-liquid phase boundary at $d \approx 0.67$ nm.

We recapitulate the interesting speculation proposed by Giovambattista *et al.*[34] that at sufficiently elevated temperatures the phase boundaries extending down to small plate separations may not collide with the $d \approx 0.40$ nm line at which water becomes immobilized between the plates, but rather terminate at a critical point prior to this intersection. Additional simulation work at higher temperatures and more closely spaced state points in d would be required to test this hypothesis. Giovambattista *et al.*[34] also speculatively proposed the existence of a triple point with coexisting, vapor, liquid, and crystalline phases.[34] The current work provides support for this conjecture and refines the estimate of the putative location of this point to [$P \approx 0.07$ GPa, $d \approx 0.67$ nm] at the intersection of the vapor, liquid and bilayer ice phases (Fig. 2). The simulations conducted in the region of state space around this point did not exhibit binary or tertiary phase coexistence, which would likely require the simulation of larger plates for longer time scales than the calculations performed in this work.[34] Furthermore, the sensitivity of the phase behavior of the system to small changes in pressure and plate separation, leads us to anticipate the search for a triple point to require a large number of simulations distributed over a finely spaced *P*-*d* grid.

Our expanded phase diagram predicts a number of interesting phase transitions, including the liquid to THF, and (f)THF to bilayer ice transitions previously observed by Giovambattista *et al.*[75] As discussed above, the structural similarity of the THF to fTHF suggests that the transition between these phases is unlikely to be a sharp first order transition, but rather a continuous change. We also observe a solid-solid phase boundary between monolayer and bilayer ices. Bai *et al.* reported the first observation of Ostwald's "rule of stages" in a two-dimensional environment, in which a metastable low density ice melted into a transient unstable liquid phase prior to recrystallization to the equilibrium high density ice phase.[43,123] It would be of interest to probe the monolayer ice-bilayer ice phase transition in the current work, to ascertain if similar behavior is observed. The monolayer liquid possesses phase boundaries with both the monolayer and bilayer ices, but along the family of isobars around $P \approx 0.15$ GPa, we observe the interesting result that the bilayer ice may be converted to the monolayer ice by passing through an intermediary equilibrium vapor phase.

Finally, our map suggests the intriguing possibility of a monolayer liquid to bilayer liquid transition if the intervening bilayer ice were to destabilize with respect to the liquid phases. Such a scenario may conceivably be achieved at elevated temperatures,[85] and might be efficiently tested by conducting replica exchange molecular dynamics over sufficiently large temperature ranges in this region of the phase diagram.[124]

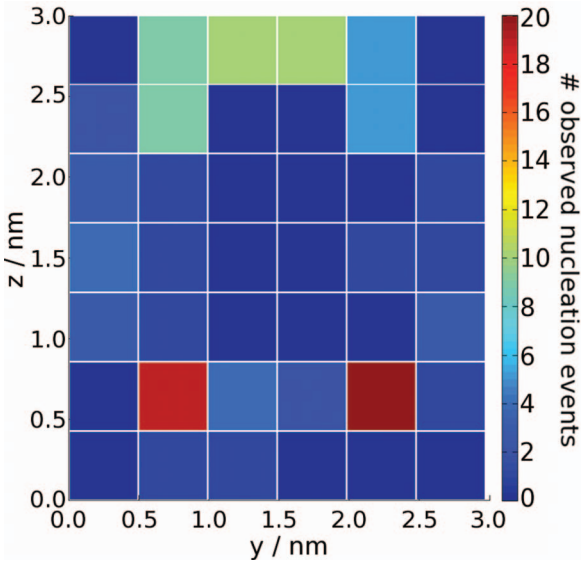

FIG. 10. Nucleation histogram for 117 bilayer ice to vapor decompression-induced sublimation runs that exhibited complete drying transitions. The gap region was discretized into cells of size [$\Delta y = 0.495$ nm, $\Delta z = 0.429$ nm], resulting in a 6×7 grid in the y,z-plane that spans the gap in the x-direction. Cell size was dictated by the geometry of the cristobalite plates (cf. Fig. 1(d)). The heat map illustrates the number of bridging cavity nucleation events observed within each cell.

B. Capillary sublimation of bilayer ice

In this section, we turn from a consideration of the phase behavior of confined water, to the analysis of a particular phase transition: decompression-induced sublimation of the confined bilayer ice. As detailed in Sec. II C, 201 simulations commencing from an equilibrated bilayer ice phase at [$P = 0.095$ GPa, $d = 0.60$ nm] were subjected to a pressure drop to (-0.025) GPa in order to move the system to the left of the phase boundary in Fig. 2, and induce drying on a nanosecond time scale. Complete transition to the equilibrium vapor phase was observed in 117 of the 201 trajectories.

Fig. 10 presents a histogram of the location of the initial local melting and nucleation of the bridging vapor cavity, collected over the 117 trajectories in which complete drying was observed. Adopting the null hypothesis of a uniform nucleation probability in each cell of the grid, Pearson's χ^2 test predicts a probability of seeing the observed nucleation distribution of less than 1 in 10^9. This result indicates that sublimation cannot be modeled as the nucleation of a bridging cavity at a random location within the gap, but rather preferentially initiates near the corner of the plates. The four corner cells with centers located $\sim$0.75 nm from each edge, accounted for over 45% of the observed nucleation events.

Application of PCA to the 201 sublimation trajectories in the manner described in Sec. II D resulted in the singular value spectrum presented in Fig. S7.[107] A spectral gap after the fifth singular value indicates that the top five PCs are required to describe the principal features of the sublimation transition, allowing approximate reconstructions of any observed occupancy vector to be formed by linear superpositions of these five vectors and the mean binary occupancy vector (cf. Eq. (1)). These six vectors are presented in Fig. 11. As we shall see, this decomposition is of great value in

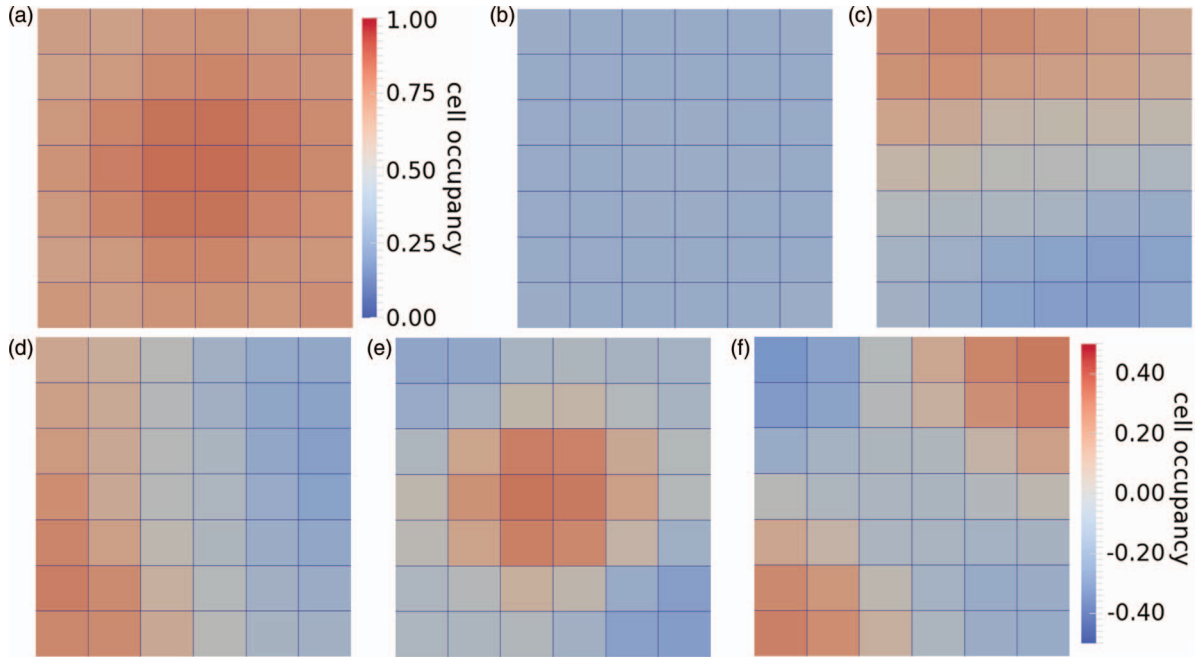

FIG. 11. The (a) mean binary occupancy vector, $\vec{v}_{mean}$, and (b)–(f) top five principal component vectors, $\vec{PC}_i$, $i = 1, \ldots, 5$, resulting from application of PCA to the ensemble of 201 decompression-induced sublimation trajectories from the bilayer crystalline solid to vapor at plate separations of $d = 0.60$ nm. Grid dimensions and orientation are identical to that presented in Fig. 1(d). The scalar value in each cell of these reconstructions may be interpreted as the average probability of that cell being occupied by at least one water molecule O atom, with the understanding that negative values are permissible in panels (b)–(f), since these probabilities do not take on meaning until a linear combination of these PCs and the mean binary occupancy vector is formed. The color bar pertaining to panel (a) is displayed directly to the right of this panel, whereas panels (b)–(f) share the color bar adjacent to panel (f).

furnishing a coherent and transparent interpretation of the sublimation process.

$\vec{PC}_1$ is an approximately uniform vector, corresponding to global, homogeneous drying throughout the gap region. The structure of $\vec{PC}_2$ corresponds to an obliquely divided plate, in which the cells occupying the extremal corner positions possess values of approximately 0.30 and (−0.30), with a smooth gradient interpolating over the remaining cells. $\vec{PC}_3$ is related to $\vec{PC}_2$ by a 90° counterclockwise rotation. $\vec{PC}_4$ has large positive values (∼0.40) in the cells at the center of the plate, small negative values elsewhere (∼(−0.20)) with slightly larger negative values (∼(−0.30)) in the top-left and bottom right corners. $\vec{PC}_5$ is approximately related to $\vec{PC}_4$ by 90° counterclockwise rotation and a sign inversion. As we have previously observed, our system is not strictly rotationally symmetric due to structural differences between the edges of the plates, and to different plate lengths in the *y* and *z*-dimensions. Nevertheless, the close relationships between $\vec{PC}_2$ and $\vec{PC}_3$, and $\vec{PC}_4$ and $\vec{PC}_5$ apparently result from the *approximate* fourfold rotational symmetry inherent in our two-dimensional treatment of the system.

We compute the binary occupancy vector associated with each snapshot harvested from the 201 evaporation trajectories and calculate the associated values of $\{\alpha_i\}_{i=1}^{5}$ by projecting this vector into the top five PCs using Eq. (1). These values allow the construction of low dimensional embeddings of each snapshot into the five-dimensional PC basis set. For clarity of visualization, in Fig. 12 we present the embedding of all snapshots into the top three PCs, and illustrate the variation of PC4 and PC5 over this embedding in Figs. S9 and S10.[107]

Each point in the embedding in Fig. 12 has been colored according to the fractional occupancy of its binary state vector, providing a measure of the number of cells in the gap that are occupied by at least one water molecule. It is clear from the heat map that the projection of a particular microstate of the system into $\vec{PC}_1$, α_1, is well-correlated with the number of inter-plate water molecules. Snapshots clustered at the dark red, low α_1 end of the lozenge-shaped point cloud correspond

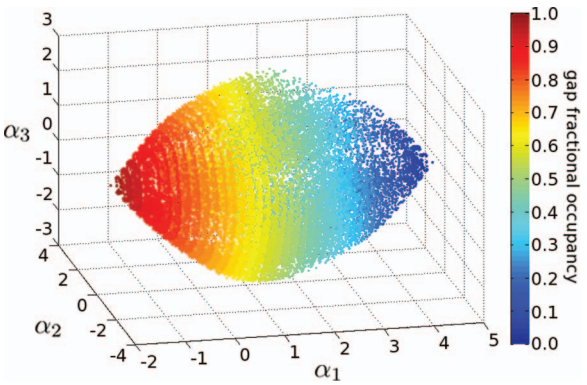

FIG. 12. Embedding of each snapshot from the 201 sublimation trajectories into the top three PCs of this data set. α_i is defined in Eq. (1) as the projection into $\vec{PC}_i$ of the binary occupancy vector associated with a particular snapshot. Each point has been colored according to the fractional occupancy of the gap in that particular snapshot, defined as the fraction of cells in Fig. 1(d) which contain at least one water molecule O atom.

to states in which the bilayer ice occupies the gap, whereas those localized at the dark blue, high α_1 tip possess a vapor-filled gap. This relationship may be anticipated from the identity of $\vec{PC}_1$ as an approximately uniform vector (Fig. 11(b)), into which the projection of a binary occupancy vector corresponding to a particular system configuration proceeds by taking the dot product. By construction, the elements of a binary occupancy vector are either 0 or 1, and a dot product with a uniform vector corresponds precisely—to within a multiplicative constant—to enumeration of the number of occupied cells in the gap.

The embedding of the sublimation trajectories into the top few PCs permits visualization of the progression of the drying transition in a low-dimensional spaces, and determination of the most probable sublimation pathways followed by the system. To more clearly identify these paths through the point cloud in Fig. 12 and reveal its internal structure, we divided the lozenge along the α_1 axis into nine slices width $\Delta\alpha_1 = 0.719$ (Fig. S8[107]). Treating each slice as quasi-two-dimensional, the probability distribution of points over the PC2-PC3 projections were computed, and are presented in Fig. 13. Each panel in this figure presents the probability distribution in the α_2-α_3 plane of the subset of snapshots with a particular range of α_1 values, ranging from wet states containing the bilayer crystal at $\alpha_1 = [-1.718, -0.999)$ in panel (a), to completely dry states at $\alpha_1 = [4.036, 4.755)$ in panel (i). These slices clearly reveal the presence of well-defined regions of high probability density, corresponding to highly populated drying pathways in the ensemble of simulation trajectories. In panels (a) and (i), there is a single probability maximum corresponding to states occupied entirely by the bilayer ice and vapor, respectively. The remaining seven panels possess four or five local maxima, and exhibit two axes of approximate symmetry, consistent with the approximate fourfold rotational symmetry of the system.

We now proceed to trace a particular sublimation pathway through the embedding to illuminate the role of the top PCs in the drying process, and the mechanistic insight they furnish. We choose to follow the high probability drying pathway passing through the local maxima indicated by the × symbols in Fig. 13. Representative snapshots were extracted at these locations and are presented in the corresponding panels in Fig. 14. A comprehensive ensemble of representative snapshots along all highly populated sublimation pathways is presented in Figs. S11 and S12.[107]

Starting from the initial state in panel (a) of Figs. 13 and 14 in which a bilayer ice occupies the gap, local melting of the ice at the top left corner leads to the nucleation of a bridging vapor cavity in (b). Here, the four local maxima are situated at approximately $[\alpha_2 = \pm 1, \alpha_3 = \pm 1]$, corresponding to roughly equal contributions of PC2 and PC3 in the PC basis set. It is clear from inspection of Fig. 11 that these four combinations may be linearly superposed with PC1 and the mean binary occupancy vector to yield representative binary occupancy vectors with low occupancy probability localized to one corner of the gap, and high occupancy probability elsewhere. Application of Pearson's χ^2 test at 5% significance shows that the null hypothesis of equal nucleation probabilities in each corner cannot be rejected, confirming the expectation that

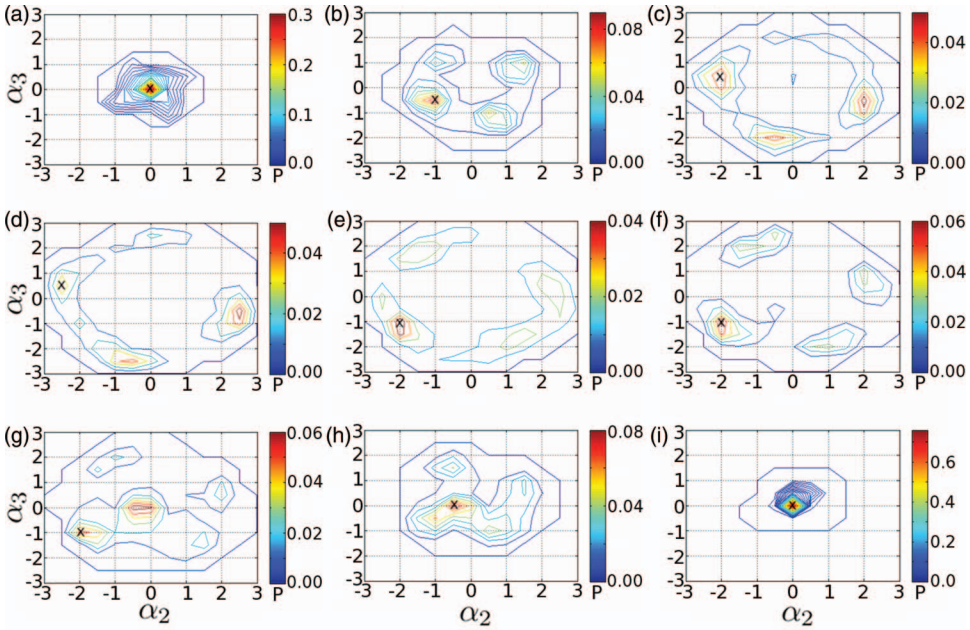

FIG. 13. To facilitate visualization of the internal structure of the three-dimensional point cloud in Fig. 12, the point cloud was cut along the axis containing its $\vec{PC}_1$ projection into nine slices over the α_1 ranges (a) [–1.718, −0.999), (b) [−0.999, −0.280), (c) [−0.280,0.440] (d) [0.440,1.159), (e) [1.159,1.878), (f) [1.878,2.597), (g) [2.597,3.316), (h) [3.316,4.036), and (i) [4.036,4.755). The two-dimensional probability distributions in this figure were generated by collecting histograms over the PC2-PC3 projection of the points in each slice (Fig. S8[107]), using cubic mesh with side length 0.5. The color bar indicates the total probability, P, residing in each cell of the mesh. Interpolative contours in P are plotted in increments of 0.01. The × symbol in each frame (a)–(i) marks the location of representative system snapshots presented in the corresponding panels of Fig. 14.

nucleation initiates with equal probability at each of the four corners.

Progressing further along the drying pathway into panel (c), we observe the expansion of the vapor cavity along one edge of the plates, with the expansion front initiating local melting of the row of bilayer hexagons at the boundary of the plates, ejecting these water molecules into the bulk. Completion of this stage of the process leaves an approximately 1 nm vapor strip along one edge of the plates, with the remainder of the gap region still occupied by the bilayer crystal. At this point, the probability maxima are approximately situated directly along the PC2 and PC3 projection axes, leading to linear combinations of the mean binary occupancy vector, $\vec{PC}_1$ and one or the other of $\vec{PC}_2$ or $\vec{PC}_3$, in which one of the four edges of the plates has dried. In this particular pathway, the cavity expanded in a clockwise direction around the plates, but of the 117 trajectories which progressed to completely dry states, 63 progressed in a clockwise and 54 in an anticlockwise direction. A χ^2 analysis at 5% significance indicated that the null hypothesis of equal splitting probabilities could not be rejected, confirming the expectation that drying proceeds with equal probability in each direction. Accordingly, the drying pathways that proceed through the four maxima in Fig. 13(b), bifurcate with approximately equal probability into the pairs of maxima flanking each of these positions in Fig. 13(c).

Passing through panel (d) and into (e), we observe the expansion of the vapor cavity along a second edge of the plates, and the attendant melting and expulsion to the bulk of another row of crystalline hexagons, leaving an approximately 2 nm × 2 nm square of bilayer ice between the plates, bounded by 1 nm vapor strips on two sides, and connected to the bulk fluid along its remaining edges. The approximate axes of symmetry have again rotated by ∼45°. In contrast to the slice in Fig. 13(b) which was taken at negative α_1 values, the α_1 range of the slice in Fig. 13(e) spans exclusively positive values. Accordingly, the binary occupancy vectors in the four local maxima constructed from the linear superposition of the mean binary occupancy vector, $\vec{PC}_1$ and approximately equal parts $\vec{PC}_2$ and $\vec{PC}_3$, possess high occupancy probabilities only in one of the four corners, with low probabilities elsewhere. At this stage of drying, we observe a second bifurcation of pathways passing through each of the four maxima in Fig. 13(d) into the two maxima on either side of these locations in Fig. 13(e). Physically, this corresponds to splitting into a *branching* path, in which the two dry edges emanate from the corner at which nucleation initiated, or a *sequential* path, in which the cavity propagates along two contiguous edges. We observe a statistically significant (χ^2 test, $p = 0.05$) preference for branching, with 60% of sublimation trajectories partitioning into this route, and is the course followed by the pathway that we trace into panel (e).

Progressing to panels (f) and (g), we observe melting of the crystalline order in the promontory of bilayer ice extending into the gap, and its recession into the bulk fluid. In most trajectories the expulsion of the remaining confined water proceeds collectively in a single step, but in approximately 1 in 4 trajectories, the outer edge of this region evacuates into the bulk, leaving a small cluster of molecules isolated in the center of the plates as illustrated in Fig. 14(h). It is possible that these isolated clusters are an artifact of the large pressure drops employed to induce sublimation, whereby rapid evacuation of the molecules near the edge of the plates induces

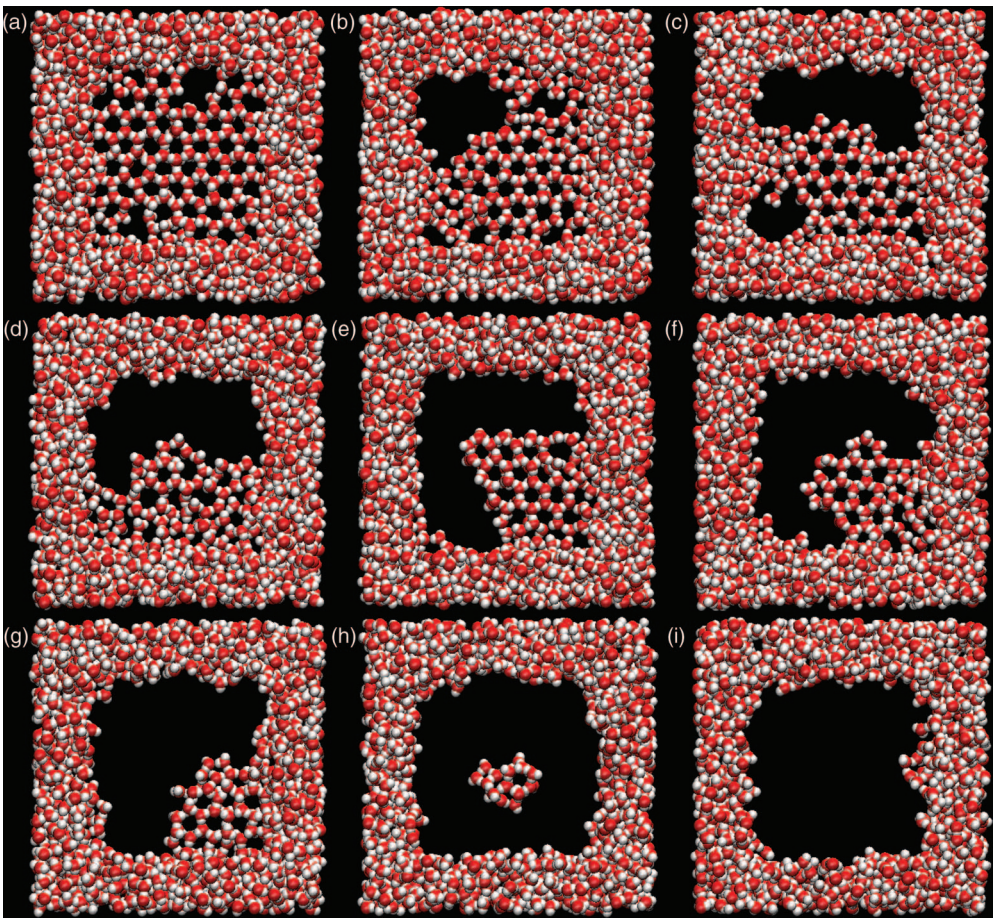

FIG. 14. Sequence of nine system snapshots illustrating the progression of drying from the (a) bilayer ice to (i) vapor phase. The plates have been removed from view to better show the gap region. The process commences by the nucleation of a vapor cavity near one corner of the plates, which proceeds to expand down one side, and then another, leaving a promontory of bilayer ice extending into the gap region. Drying completes when this promontory undergoes fluctuation induced melting and recedes into the bulk fluid. In some trajectories, a small island of water molecules transiently exists the center of the gap, as shown in panel (h). These snapshots were selected as representative configurations extracted at the locations indicated by × symbols in the corresponding panels in Fig. 13.

separation of the central island. Nevertheless, only one simulation exhibited an isolated island between the plates at the end of the 2 ns drying trajectory, suggesting that these structures are unstable on nanosecond time scales. This less common route corresponds to the evaporation pathway tracing a route from one of the four exterior local maxima in Fig. 13(f) to the central maximum at approximately $[\alpha_2 = 0, \alpha_3 = 0]$ in Figs. 13(g) and 13(h). At this location, $\vec{PC}_2$ and $\vec{PC}_3$ do not contribute significantly to the linear superposition, and it is through the contributions of $\vec{PC}_4$ that the binary occupancy vector constructed in the PC basis is able to capture such configurations. As illustrated in Fig. S9,[107] α_4 becomes large in the central regions of panels (d)–(h). The contributions of $\vec{PC}_5$ throughout the drying transition are illustrated in Fig. S10,[107] with the primary role being to sharpen the relatively diffuse boundaries between wet and dry regions that result from superpositions of $\vec{PC}_2$ and $\vec{PC}_3$ alone.

Evaporation completes in panel (i), where all trajectories coalesce to the single probability maximum and a continuous vapor phase occupies the gap. The only significant contribution to the binary occupancy vector in the top five PCs is a large, positive α_1, which serves to cancel out the mean binary occupancy vector, leaving a nearly uniform binary occupancy vector with the occupancy probability of all elements near zero. A movie illustrating the drying transition in one particular molecular dynamics trajectory (Movie S1), and an accompanying movie showing the abstraction of this trajectory to occupancy vectors (Movie S2) are available in the supplementary material.[107]

Prior simulation work has shown that the capillary evaporation of liquid water confined between nanoscopic hydrophobic plates proceeds by the nucleation of a bridging vapor cavity that subsequently expands to fill the gap.[1,3,50,51,54,56,58] Our findings show that the capillary drying of the bilayer ice proceeds by a different mechanism, in which a bridging vapor cavity nucleates near one corner of the bilayer ice slab, expands along one, then another edge of the plates, to leave a residual promontory of ice that ultimately melts and recedes into the bulk. Our application of PCA to the analysis of this process furnished a useful framework within which to follow the sublimation transition in a low (five) dimensional space.

IV. CONCLUSIONS

The equilibrium phase behavior of nanoscale confined water plays an important role in numerous natural and

engineered systems, from the morphology of clays[4] to transport through carbon nanotubes.[7] In this work we have employed extensive molecular dynamics simulation of water confined between atomistically detailed hydrophobic plates at $T = 298$ K to synthesize a comprehensive phase diagram for gap widths of $d = 0.40$–0.80 nm and pressures of $P = (-0.1)$ to 1.0 GPa (Fig. 2). We have identified six distinct "wet" confined morphologies, the structural and dynamic equilibrium properties of which were characterized by probability distributions over the confined volume (Fig. 4), radial distribution functions (Fig. 5), and the self-diffusivity across the gap (Fig. 6).

One of the six phases we identify is a novel confined monolayer ice possessing a planar hexagonal crystal structure templated by the atoms of the confining surfaces. This phase is qualitatively distinct from crystalline monolayers previously reported in the literature,[43,111] and resembles the theoretically predicted structure of a non-dissociated adsorbed monolayer on a Ru(0001) surface.[116,117] It would be of interest to perform simulations employing infinite parallel plates to verify whether this phase is capable of supporting the long range crystalline order previously observed in bilayer ices.[42,75] Restriction to a planar monolayer permits each constituent water molecule to participate in only three in-plane hydrogen bonds, prohibiting this structure from obeying the bulk ice rules.[110] Geometric considerations dictate that the hydrogen bond arrangement must contain at least one unsatisfied hydrogen bond donor per hexagon in the lattice, predicting ~27% of donors to be unsatisfied in a lattice of the size considered in this work. The measured value of 33.3% suggests that the hydrogen bonding network is nearly optimally arranged. The residual entropy imparted to the structure by the unsatisfied donors is nearly twice that of bulk I_h ice, providing an entropic stabilization of this phase.

Our phase diagram provides additional support for the conjecture of Giovambattista *et al.*[34] that at sufficiently high temperatures, the phase boundaries extending down to small plate separations may terminate at a critical point prior to the water molecules becoming immobilized between the plates. These authors also speculated upon the existence of a triple point, the location of which the current study has refined to the immediate vicinity of [$P \approx 0.07$ GPa, $d \approx 0.67$ nm], with coexisting vapor, liquid and bilayer ice phases. Additional simulations over a more tightly spaced *P-d* grid at higher temperatures in the first instance, and employing larger plates in the second, would be required to further substantiate each of these two conjectures.

A natural extension of this work would be to compute the phase diagram presented in Fig. 2 at different temperatures, permitting the construction of a three-dimensional phase diagram in *P-T-d*. It would be of interest to investigate whether the intriguing crystalline and quasi-crystalline bilayer ices observed in simulations by Johnston *et al.* might emerge in lower temperature simulations of this system.[42] Similarly, it would be intriguing to assess whether the buckled monolayer of Zangi and Mark[111] or the Archimedean 4×8^2 truncated square monolayer of Bai *et al.*[43] might be supported in this system.

In this work we present the first investigation of sublimation of a bilayer ice confined between two atomistically detailed hydrophobic plates at nanometer separations by simulating hundreds of decompression-induced sublimation transitions. Application of PCA facilitated the synthesis of low-dimensional descriptions of the drying trajectories and the development of mechanistic insight. This analysis revealed sublimation to initiate by the nucleation of a vapor cavity at one corner of the crystalline slab. The cavity subsequently expands along a 1 nm wide strip along one edge of the plates, ejecting water molecules into the bulk, followed by propagation along a second edge, leaving a promontory of bilayer ice bounded by vapor on two sides and connected to the bulk along the remaining two edges. Fluctuation-induced melting of the crystalline order releases the constituent water molecules from the lattice, and leads to recession of the remaining inter-plate water molecules into the bulk fluid. Infrequently, this process leaves a small cluster of isolated water molecules in the center of the plates that eventually migrates into the bulk. It would be of interest to study drying in larger plates, where we speculate that increasing linear distances between the center of the plates and the bulk may favor the development of long-lived islands of bilayer ice, or infinite plates, lacking the corner regions where nucleation was observed to preferentially initiate.

Evaporation of the confined liquid is known to proceed by the formation and expansion of a bridging vapor cavity,[1,3,50,51,54,56,58] resulting in the collective compression and expulsion into the bulk of the water molecules residing within the gap. In contrast, cavitation in the bilayer ice is restricted to proceed at the corners of the plates where there is direct access to the bulk fluid. We propose that the incompressibility of the bilayer ice lattice, together with the low mobility of the constituent molecules, underlie the qualitative differences in the drying mechanism.

The evaporative transitions in the current study were triggered by the application of a pressure drop to render the initially wet system metastable with respect to the vapor phase. Drying could alternatively be induced by reducing the width of the gap by pushing the silica plates together,[125] causing the system to traverse the phase boundary in Fig. 2 vertically, rather than horizontally. Bolhuis and Chandler have previously speculated that mobile plates may reduce the activation barrier to drying compared to the static plate scenario,[50] and it would be of interest to determine whether the decompression-induced drying mechanisms determined in this work are conserved under narrowing-induced drying.

Finally, this work considered the sublimation mechanism of a confined bilayer ice, but did not attempt to quantify sublimation rates or identify the transition state ensemble. Recent work by Sharma and Debenedetti employed forward flux sampling to evaluate the rates and transition states of capillary evaporation of confined liquid water,[56] and we propose that this or similar path sampling techniques may be readily applied to the sublimation transition.[126–129]

In this work, we have reported a significant expansion of the phase diagram of confined water, identified a novel monolayer ice phase, and identified the structural mechanism for the capillary sublimation of a confined bilayer ice. We believe

that these findings will be of value in advancing the basic understanding of the thermodynamics and dynamics of scientifically interesting and technologically important confined water systems.

ACKNOWLEDGMENTS

We thank I. G. Kevrekidis for useful discussions. N.G. gratefully acknowledges support from a PSC-CUNY Award, jointly funded by The Professional Staff Congress and The City University of New York. P.J.R. gratefully acknowledges the support of the National Science Foundation (Collaborative Research Grants No. CHE0910615) and the R. A. Welch Foundation (F0019). A.Z.P. gratefully acknowledges support from the Department of Energy, Office of Basic Energy Sciences (Grant No. DE-SC-0002128). P.G.D. gratefully acknowledges the support of the National Science Foundation (Grants CHE-0908265 and CHE-1213343).

[1]X. Huang, C. J. Margulis, and B. J. Berne, "Dewetting-induced collapse of hydrophobic particles," Proc. Natl. Acad. Sci. U.S.A. **100**, 11953 (2003).
[2]K. Lum, D. Chandler, and J. D. Weeks, "Hydrophobicity at small and large length scales," J. Phys. Chem. B **103**, 4570 (1999).
[3]N. Choudhury and B. M. Pettitt, "The dewetting transition and the hydrophobic effect," J. Am. Chem. Soc. **129**, 4847 (2007).
[4]R. M. Barrer, *Zeolites and Clay Minerals as Sorbents and Molecular Sieves* (Academic, 1978).
[5]H. E. Warriner, S. H. J. Idziak, N. L. Slack, P. Davidson, and C. R. Safinya, "Lamellar biogels: fluid-membrane-based hydrogels containing polymer lipids," Science **271**, 969 (1996).
[6]C. Peter and G. Hummer, "Ion transport through membrane-spanning nanopores studied by molecular dynamics simulations and continuum electrostatics calculations," Biophys. J. **89**, 2222 (2005).
[7]G. Hummer, J. C. Rasaiah, and J. P. Noworyta, "Water conduction through the hydrophobic channel of a carbon nanotube," Nature (London) **414**, 188 (2001).
[8]J. C. Rasaiah, S. Garde, and G. Hummer, "Water in nonpolar confinement: From nanotubes to proteins and beyond," Annu. Rev. Phys. Chem. **59**, 713 (2008).
[9]A. A. Darhuber and S. M. Troian, "Principles of microfluidic actuation by modulation of surface stresses," Annu. Rev. Fluid Mech. **37**, 425 (2005).
[10]F. Olofson, S. Badiei, and L. Holmlid, "Adsorbed water molecules on a K-promoted catalyst surface studied by stimulated micro-Raman spectroscopy," Langmuir **19**, 5756 (2003).
[11]D. Landolt, *Corrosion and Surface Chemistry of Metals* (CRC, 2007).
[12]M. S. Cheung, A. E. García, and J. N. Onuchic, "Protein folding mediated by solvation: water expulsion and formation of the hydrophobic core occur after the structural collapse," Proc. Natl. Acad. Sci. U.S.A. **99**, 685 (2002).
[13]T. M. Truskett, P. G. Debenedetti, and S. Torquato, "Thermodynamic implications of confinement for a waterlike fluid," J. Chem. Phys. **114**, 2401 (2001).
[14]P. Kumar, S. V. Buldyrev, F. W. Starr, N. Giovambattista, and H. E. Stanley, "Thermodynamics, structure, and dynamics of water confined between hydrophobic plates," Phys. Rev. E **72**, 051503 (2005).
[15]P. G. Debenedetti, "Supercooled and glassy water," J. Phys. Condens. Matter **15**, R1669 (2003).
[16]C. Kim, B. Barstow, M. W. Tate, and S. M. Gruner, "Evidence for liquid water during the high-density to low-density amorphous ice transition," Proc. Natl. Acad. Sci. U.S.A. **106**, 4596 (2009).
[17]C. A. Angell, "Insights into phases of liquid water from study of its unusual glass-forming properties," Science **319**, 582 (2008).
[18]O. Mishima and H. E. Stanley, "The relationship between liquid, supercooled and glassy water," Nature (London) **396**, 329 (1998).
[19]F. H. Stillinger, "Structure in aqueous solutions of nonpolar solutes from the standpoint of scaled-particle theory," J. Solution Chem. **2**, 141 (1973).
[20]D. Chandler, "Interfaces and the driving force of hydrophobic assembly," Nature (London) **437**, 640 (2005).
[21]P. R. ten Wolde and D. Chandler, "Drying-induced hydrophobic polymer collapse," Proc. Natl. Acad. Sci. U.S.A. **99**, 6539 (2002).
[22]T. F. Miller, E. Vanden-Eijnden, and D. Chandler, "Solvent coarse-graining and the string method applied to the hydrophobic collapse of a hydrated chain," Proc. Natl. Acad. Sci. U.S.A. **104**, 14559 (2007).
[23]A. L. Ferguson, P. G. Debenedetti, and A. Z. Panagiotopoulos, "Solubility and molecular conformations of n-alkane chains in water," J. Phys. Chem. B **113**, 6405 (2009).
[24]A. L. Ferguson, A. Z. Panagiotopoulos, P. G. Debenedetti, and I. G. Kevrekidis, "Systematic determination of order parameters for chain dynamics using diffusion maps," Proc. Natl. Acad. Sci. U.S.A. **107**, 13597 (2010).
[25]A. Luzar and K. Leung, "Dynamics of capillary evaporation. I. Effect of morphology of hydrophobic surfaces," J. Chem. Phys. **113**, 5836 (2000).
[26]K. A. Dill, "Dominant forces in protein folding," Biochemistry **29**, 7133 (1990).
[27]R. Zhou, X. Huang, C. J. Margulis, and B. J. Berne, "Hydrophobic collapse in multidomain protein folding," Science **305**, 1605 (2004).
[28]T. Young, L. Hua, X. Huang, R. Abel, R. Friesner, and B. J. Berne, "Dewetting transitions in protein cavities," Proteins: Struct., Funct., Bioinf. **78**, 1856 (2010).
[29]N. Giovambattista, C. F. Lopez, P. J. Rossky, and P. G. Debenedetti, "Hydrophobicity of protein surfaces: Separating geometry from chemistry," Proc. Natl. Acad. Sci. U.S.A. **105**, 2274 (2008).
[30]P. Liu, X. Huang, R. Zhou, and B. J. Berne, "Observation of a dewetting transition in the collapse of the melittin tetramer," Nature (London) **437**, 159 (2005).
[31]Z. Yang, B. Shi, H. Lu, P. Xiu, and R. Zhou, "Dewetting transitions in the self-assembly of two amyloidogenic β-sheets and the importance of matching surfaces," J. Phys. Chem. B **115**, 11137 (2011).
[32]A. Luzar, D. Bratko, and L. Blum, "Monte Carlo simulation of hydrophobic interaction," J. Chem. Phys. **86**, 2955 (1987).
[33]D. R. Bérard, P. Attard, and G. N. Patey, "Cavitation of a Lennard-Jones fluid between hard walls, and the possible relevance to the attraction measured between hydrophobic surfaces," J. Chem. Phys. **98**, 7236 (1993).
[34]N. Giovambattista, P. J. Rossky, and P. G. Debenedetti, "Effect of pressure on the phase behavior and structure of water confined between nanoscale hydrophobic and hydrophilic plates," Phys. Rev. E **73**, 041604 (2006).
[35]C. Cerdeiriña, P. Debenedetti, P. Rossky, and N. Giovambattista, "Evaporation length scales of confined water and some common organic liquids," J. Phys. Chem. Lett. **2**, 1000 (2011).
[36]A. Wallqvist and B. J. Berne, "Computer simulation of hydrophobic hydration forces on stacked plates at short range," J. Phys. Chem. **99**, 2893 (1995).
[37]J. Li, T. Liu, X. Li, L. Ye, H. Chen, H. Fang, Z. Wu, and R. Zhou, "Hydration and dewetting near graphite-CH3 and graphite-COOH plates," J. Phys. Chem. B **109**, 13639 (2005).
[38]D. Bratko, R. A. Curtis, H. W. Blanch, and J. M. Prausnitz, "Interaction between hydrophobic surfaces with metastable intervening liquid," J. Chem. Phys. **115**, 3873 (2001).
[39]N. Choudhury and B. M. Pettitt, "Enthalpy-entropy contributions to the potential of mean force of nanoscopic hydrophobic solutes," J. Phys. Chem. B **110**, 8459 (2006).
[40]N. Choudhury, "On the manifestation of hydrophobicity at the nanoscale," J. Phys. Chem. B **112**, 6296 (2008).
[41]I. Brovchenko, A. Geiger, and A. Oleinikova, "Water in nanopores. I. Coexistence curves from Gibbs ensemble Monte Carlo simulations," J. Chem. Phys. **120**, 1958 (2004).
[42]J. C. Johnston, N. Kastelowitz, and V. Molinero, "Liquid to quasicrystal transition in bilayer water," J. Chem. Phys. **133**, 154516 (2010).
[43]J. Bai, C. A. Angell, and X. C. Zeng, "Guest-free monolayer clathrate and its coexistence with two-dimensional high-density ice," Proc. Natl. Acad. Sci. U.S.A. **107**, 5718 (2010).
[44]L. Hua, R. Zangi, and B. J. Berne, "Hydrophobic interactions and dewetting between plates with hydrophobic and hydrophilic domains," J. Phys. Chem. C **113**, 5244 (2009).
[45]N. Giovambattista, P. G. Debenedetti, and P. J. Rossky, "Hydration behavior under confinement by nanoscale surfaces with patterned hydrophobicity and hydrophilicity," J. Phys. Chem. C **111**, 1323 (2007).
[46]T. Koishi, S. Yoo, K. Yasuoka, X. C. Zeng, T. Narumi, R. Susukita, A. Kawai, H. Furusawa, A. Suenaga, N. Okimoto, N. Futatsugi, and T. Ebisuzaki, "Nanoscale hydrophobic interaction and nanobubble nucleation," Phys. Rev. Lett. **93**, 185701 (2004).
[47]T. Koishi, K. Yasuoka, T. Ebisuzaki, S. Yoo, and X. C. Zeng, "Large-scale molecular-dynamics simulation of nanoscale hydrophobic interaction and nanobubble formation," J. Chem. Phys. **123**, 204707 (2005).

[48] A. P. Willard and D. Chandler, "Coarse-grained modeling of the interface between water and heterogeneous surfaces," Faraday Discuss. **141**, 209 (2008).
[49] J. Mittal and G. Hummer, "Interfacial thermodynamics of confined water near molecularly rough surfaces," Faraday Discuss. **146**, 341 (2010).
[50] P. G. Bolhuis and D. Chandler, "Transition path sampling of cavitation between molecular scale solvophobic surfaces," J. Chem. Phys. **113**, 8154 (2000).
[51] K. Leung, A. Luzar, and D. Bratko, "Dynamics of capillary drying in water," Phys. Rev. Lett. **90**, 65502 (2003).
[52] K. Leung and A. Luzar, "Dynamics of capillary evaporation. II. Free energy barriers," J. Chem. Phys. **113**, 5845 (2000).
[53] A. Luzar, "Activation barrier scaling for the spontaneous evaporation of confined water," J. Phys. Chem. B **108**, 19859 (2004).
[54] K. Lum and A. Luzar, "Pathway to surface-induced phase transition of a confined fluid," Phys. Rev. E **56**, 6283 (1997).
[55] L. Xu and V. Molinero, "Liquid-vapor oscillations of water nanoconfined between hydrophobic disks: Thermodynamics and kinetics," J. Phys. Chem. B **114**, 7320 (2010).
[56] S. Sharma and P. G. Debenedetti, "Evaporation rate of water in hydrophobic confinement," Proc. Natl. Acad. Sci. U.S.A. **109**, 4365 (2012).
[57] K. Lum and D. Chandler, "Phase diagram and free energies of vapor films and tubes for a confined fluid," Int. J. Thermophys. **19**, 845 (1998).
[58] P. Ball, "Chemical physics – how to keep dry in water," Nature (London) **423**, 25 (2003).
[59] R. M. Pashley, P. M. McGuiggan, B. W. Ninham, and D. F. Evans, "Attractive forces between uncharged hydrophobic surfaces: direct measurements in aqueous solution," Science **229**, 1088 (1985).
[60] H. K. Christenson and P. M. Claesson, "Cavitation and the interaction between macroscopic hydrophobic surfaces," Science **239**, 390 (1988).
[61] J. L. Parker, P. M. Claesson, and P. Attard, "Bubbles, cavities, and the long-ranged attraction between hydrophobic surfaces," J. Phys. Chem. **98**, 8468 (1994).
[62] J. W. G. Tyrrell and P. Attard, "Images of nanobubbles on hydrophobic surfaces and their interactions," Phys. Rev. Lett. **87**, 176104 (2001).
[63] H. K. Christenson and P. M. Claesson, "Direct measurements of the force between hydrophobic surfaces in water," Adv. Colloid Interface Sci. **91**, 391 (2001).
[64] R. Steitz, T. Gutberlet, T. Hauss, B. Klösgen, R. Krastev, S. Schemmel, A. C. Simonsen, and G. H. Findenegg, "Nanobubbles and their precursor layer at the interface of water against a hydrophobic substrate," Langmuir **19**, 2409 (2003).
[65] T. R. Jensen, M. Ø. Jensen, N. Reitzel, K. Balashev, G. H. J. Peters, K. Kjaer, and T. Bjørnholm, "Water in contact with extended hydrophobic surfaces: Direct evidence of weak dewetting," Phys. Rev. Lett. **90**, 086101 (2003).
[66] Y. H. Tsao, S. X. Yang, D. F. Evans, and H. Wennerstroem, "Interactions between hydrophobic surfaces. Dependence on temperature and alkyl chain length," Langmuir **7**, 3154 (1991).
[67] V. Yaminsky and S. Ohnishi, "Physics of hydrophobic cavities," Langmuir **19**, 1970 (2003).
[68] E. E. Meyer, Q. Lin, T. Hassenkam, E. Oroudjev, and J. N. Israelachvili, "Origin of the long-range attraction between surfactant-coated surfaces," Proc. Natl. Acad. Sci. U.S.A. **102**, 6839 (2005).
[69] E. E. Meyer, K. J. Rosenberg, and J. Israelachvili, "Recent progress in understanding hydrophobic interactions," Proc. Natl. Acad. Sci. U.S.A. **103**, 15739 (2006).
[70] E. Lindahl, B. Hess, and D. van der Spoel, "GROMACS 3.0: A package for molecular simulation and trajectory analysis," J. Mol. Model. **7**, 306 (2001).
[71] D. van der Spoel, E. Lindahl, B. Hess, G. Groenhof, A. E. Mark, and H. J. C. Berendsen, "GROMACS: Fast, flexible, and free," J. Comput. Chem. **26**, 1701 (2005).
[72] R. K. Iler, *Chemistry of Silica–Solubility, Polymerization, Colloid and Surface Properties, and Biochemistry* (Wiley, New York, 1979).
[73] C. Hammond, *The Basics of Crystallography and Diffraction* (Oxford University Press, Oxford, 2001).
[74] W. Humphrey, A. Dalke, and K. Schulten, "VMD – visual molecular dynamics," J. Mol. Graphics **14**, 33 (1996).
[75] N. Giovambattista, P. J. Rossky, and P. G. Debenedetti, "Phase transitions induced by nanoconfinement in liquid water," Phys. Rev. Lett. **102**, 50603 (2009).
[76] H. J. C. Berendsen, J. R. Grigera, and T. P. Straatsma, "The missing term in effective pair potentials," J. Phys. Chem. **91**, 6269 (1987).
[77] M. P. Allen and D. J. Tildesley, *Computer Simulations of Liquids* (Oxford University Press, New York, 1989).
[78] S. H. Lee and P. J. Rossky, "A comparison of the structure and dynamics of liquid water at hydrophobic and hydrophilic surfaces – a molecular dynamics simulation study," J. Chem. Phys. **100**, 3334 (1994).
[79] S. Nosé, "A unified formulation of the constant temperature molecular dynamics methods," J. Chem. Phys. **81**, 511 (1984).
[80] W. G. Hoover, "Canonical dynamics: Equilibrium phase-space distributions," Phys. Rev. A **31**, 1695 (1985).
[81] H. J. C. Berendsen, J. P. M. Postma, W. F. van Gunsteren, A. DiNola, and J. R. Haak, "Molecular dynamics with coupling to an external bath," J. Chem. Phys. **81**, 3684 (1984).
[82] D. van der Spoel, E. Lindahl, B. Hess, A. R. van Buuren, E. Apol, P. J. Meulenhoff, D. P. Tieleman, A. L. T. M. Sijbers, K. A. Feenstra, R. van Drunen, and H. J. C. Berendsen, *Gromacs User Manual*, version 3.3, Zürich, Groningen (2005), see www.gromacs.org.
[83] D. Frenkel and B. Smit, *Understanding Molecular Simulation: From Algorithms to Applications* (Academic, San Diego, 2002).
[84] U. Essmann, L. Perera, M. L. Berkowitz, T. Darden, H. Lee, and L. G. Pedersen, "A smooth particle mesh Ewald method," J. Chem. Phys. **103**, 8577 (1995).
[85] R. Zangi, "Water confined to a slab geometry: A review of recent computer simulation studies," J. Phys. Condens. Matter **16**, S5371 (2004).
[86] P. Liu, E. Harder, and B. J. Berne, "On the calculation of diffusion coefficients in confined fluids and interfaces with an application to the liquid-vapor interface of water," J. Phys. Chem. B **108**, 6595 (2004).
[87] S. R. V. Castrillón, N. Giovambattista, I. A. Aksay, and P. G. Debenedetti, "Evolution from surface-influenced to bulk-like dynamics in nanoscopically confined water," J. Phys. Chem. B **113**, 7973 (2009).
[88] I. T. Jolliffe, *Principal Component Analysis*, 2nd ed. (Springer, New York, 2002).
[89] T. Ichiye and M. Karplus, "Collective motions in proteins: a covariance analysis of atomic fluctuations in molecular dynamics and normal mode simulations," Proteins: Struct., Funct., Genet. **11**, 205 (1991).
[90] A. E. García, "Large-amplitude nonlinear motions in proteins," Phys. Rev. Lett. **68**, 2696 (1992).
[91] A. Amadei, A. B. M. Linssen, and H. J. C. Berendsen, "Essential dynamics of proteins," Proteins: Struct., Funct., Genet. **17**, 412 (1993).
[92] R. G. Littlejohn and M. Reinsch, "Gauge fields in the separation of rotations and internal motions in the n-body problem," Rev. Mod. Phys. **69**, 213 (1997).
[93] P. Holmes, J. L. Lumley, and G. Berkooz, *Turbulence, Coherent Structures, Dynamical Systems and Symmetry* (Cambridge University Press, 1998), Chap. 3.
[94] L. Sirovich, "Turbulence and the dynamics of coherent structures. Part I: Coherent structures," Q. Appl. Math. **45**, 561 (1987).
[95] L. Sirovich and M. Kirby, "Low-dimensional procedure for the characterization of human faces," J. Opt. Soc. Am. A **4**, 519 (1987).
[96] A. L. Ferguson, S. Zhang, I. Dikiy, A. Z. Panagiotopoulos, P. G. Debenedetti, and A. J. Link, "An experimental and computational investigation of spontaneous lasso formation in microcin J25," Biophys. J. **99**, 3056 (2010).
[97] M. Agarwal, M. P. Alam, and C. Chakravarty, "Thermodynamic, diffusional, and structural anomalies in rigid-body water models," J. Phys. Chem. B **115**, 6935 (2011).
[98] J. L. F. Abascal and C. Vega, "A general purpose model for the condensed phases of water: TIP4P/2005," J. Chem. Phys. **123**, 234505 (2005).
[99] A. Adamson, *Physical Chemistry of Surfaces*, 5th ed. (Wiley, New York, NY, 1990).
[100] *Perry's Chemical Engineers' Handbook*, 7th ed., edited by R. H. Perry and D. W. Green (McGraw-Hill, New York, NY, 1997).
[101] W. Haynes, ed., *CRC Handbook of Chemistry and Physics*, 92nd ed. (CRC Press/Taylor and Francis, Boca Raton, FL, 2012).
[102] N. Giovambattista, P. J. Rossky, and P. G. Debenedetti, "Effect of temperature on the structure and phase behavior of water confined by hydrophobic, hydrophilic, and heterogeneous surfaces," J. Phys. Chem. B **113**, 13723 (2009).
[103] K. Koga, X. C. Zeng, and H. Tanaka, "Freezing of confined water: A bilayer ice phase in hydrophobic nanopores," Phys. Rev. Lett. **79**, 5262 (1997).
[104] K. Koga, H. Tanaka, and X. C. Zeng, "First-order transition in confined water between high-density liquid and low-density amorphous phases," Nature (London) **408**, 564 (2000).

[105]F. Franks, *Water: A Matrix of Life*, 2nd ed. (Royal Society of Chemistry, Great Britain, 2000).
[106]K. T. Wikfeldt, M. Leetmaa, A. Mace, A. Nilsson, and L. G. M. Pettersson, "Oxygen-oxygen correlations in liquid water: Addressing the discrepancy between diffraction and extended X-ray absorption fine-structure using a novel multiple-data set fitting technique," J. Chem. Phys. **132**, 104513 (2010).
[107]See supplementary material at http://dx.doi.org/10.1063/1.4755750 for 12 figures showing simulation snapshots of the confined phases, the PCA singular value spectrum, additional PCA embedding visualizations, and representative snapshots of the capillary sublimation process, and two movies showing a molecular dynamics trajectory of a decompression-induced sublimation event, and the coarse-grained abstraction of the trajectory to occupancy vectors.
[108]A. Kalra, S. Garde, and G. Hummer, "Lubrication by molecularly thin water films confined between nanostructured membranes," Eur. Phys. J. Spec. Top. **189**, 147 (2010).
[109]D. Swiatla-Wojcik, "Evaluation of the criteria of hydrogen bonding in highly associated liquids," Chem. Phys. **342**, 260 (2007).
[110]K. Koga, G. T. Gao, H. Tanaka, and X. C. Zeng, "Formation of ordered ice nanotubes inside carbon nanotubes," Nature (London) **412**, 802 (2001).
[111]R. Zangi and A. E. Mark, "Monolayer ice," Phys. Rev. Lett. **91**, 25502 (2003).
[112]M. Mahoney and W. Jorgensen, "A five-site model for liquid water and the reproduction of the density anomaly by rigid, nonpolarizable potential functions," J. Chem. Phys. **112**, 8910 (2000).
[113]K. Koga and H. Tanaka, "Phase diagram of water between hydrophobic surfaces," J. Chem. Phys. **122**, 104711 (2005).
[114]C. Spagnoli, K. Loos, A. Ulman, and M. K. Cowman, "Imaging structured water and bound polysaccharide on mica surface at ambient temperature," J. Am. Chem. Soc. **125**, 7124 (2003).
[115]J. Yang, S. Meng, L. F. Xu, and E. G. Wang, "Ice tessellation on a hydroxylated silica surface," Phys. Rev. Lett. **92**, 146102 (2004).
[116]A. Hodgson and S. Haq, "Water adsorption and the wetting of metal surfaces," Surf. Sci. Rep. **64**, 381 (2009).
[117]G. Held and D. Menzel, "The structure of the p($\sqrt{3}\times\sqrt{3}$)R30° bilayer of D_2 O on Ru(001)," Surf. Sci. **316**, 92 (1994).
[118]D. Menzel, "Water on a metal surface," Science **295**, 58 (2002).
[119]P. J. Feibelman and A. Alavi, "Entropy of H_2O wetting layers," J. Phys. Chem. B **108**, 14362 (2004).
[120]L. Pauling, "The structure and entropy of ice and of other crystals with some randomness of atomic arrangement," J. Am. Chem. Soc. **57**, 2680 (1935).
[121]A. Kalra, S. Garde, and G. Hummer, "Osmotic water transport through carbon nanotube membranes," Proc. Natl. Acad. Sci. U.S.A. **100**, 10175 (2003).
[122]J. D. Porter and A. S. Zinn-Warner, "Young's modulus of two-dimensional ice from the electrostatic compression of mercury/water/mercury tunnel junctions," Phys. Rev. Lett. **73**, 2879 (1994).
[123]W. Ostwald, "Studien über die bildung und umwandlung fester körper," Z. Phys. Chem. **22**, 289 (1897).
[124]Y. Sugita and Y. Okamoto, "Replica-exchange molecular dynamics method for protein folding," Chem. Phys. Lett. **314**, 141 (1999).
[125]R. Zangi and A. E. Mark, "Bilayer ice and alternate liquid phases of confined water," J. Chem. Phys. **119**, 1694 (2003).
[126]P. G. Bolhuis, D. Chandler, C. Dellago, and P. L. Geissler, "Transition path sampling: Throwing ropes over rough mountain passes, in the dark," Annu. Rev. Phys. Chem. **53**, 291 (2002).
[127]L. Maragliano, A. Fischer, E. Vanden-Eijnden, and G. Ciccotti, "String method in collective variables: Minimum free energy paths and isocommittor surfaces," J. Chem. Phys. **125**, 024106 (2006).
[128]R. J. Allen, D. Frenkel, and P. R. ten Wolde, "Forward flux sampling-type schemes for simulating rare events: Efficiency analysis," J. Chem. Phys. **124**, 194111 (2006).
[129]F. A. Escobedo, E. E. Borrero, and J. C. Araque, "Transition path sampling and forward flux sampling. Applications to biological systems," J. Phys. Condens. Matter **21**, 333101 (2009).